Experimental investigation of the Jahn-Teller effect in the ground and excited electronic states of the tropyl radical. Part II. Vibrational analysis of the $\tilde{A}\,^2E_3''\text{-}\tilde{X}\,^2E_2''$ electronic transition

Ilias Sioutis, Vadim L. Stakhursky, György Tarczay,[a] and Terry A. Miller[b]

Laser Spectroscopy Facility, Department of Chemistry, The Ohio State University, 120 W. 18th Avenue, Columbus, Ohio 43210, USA

Laser-induced fluorescence (LIF) and laser-excited dispersed fluorescence (LEDF) spectra of the cycloheptatrienyl (tropyl) radical C_7H_7 have been observed under supersonic jet-cooling conditions. Assignment of the LIF excitation spectrum yields detailed information about the $\tilde{A}$-state vibronic structure. The LEDF emission was collected by pumping different vibronic bands of the $\tilde{A}\,^2E_3'' \leftarrow \tilde{X}\,^2E_2''$ electronic spectrum. Analysis of the LEDF spectra yields valuable information about the vibronic levels of the $\tilde{X}\,^2E_2''$ state. The $\tilde{X}$- and $\tilde{A}$-state vibronic structures characterize the Jahn-Teller distortion of the respective potential energy surfaces. A thorough analysis reveals observable Jahn-Teller activity in three of the four e_3' modes for the $\tilde{X}\,^2E_2''$ state and two of the three e_1' modes for the $\tilde{A}\,^2E_3''$ state and provides values for their deperturbed vibrational frequencies as well as linear Jahn-Teller coupling constants. The molecular parameters characterizing the Jahn-Teller interaction in the $\tilde{X}$ and $\tilde{A}$ states of C_7H_7 are compared to theoretical results and to those previously obtained for C_5H_5 and $C_6H_6^+$. © *2008 American Institute of Physics.* [DOI: 10.1063/1.2829471]

I. INTRODUCTION

The cycloheptatrienyl (tropylium) cation c-$C_7H_7^+$ is a prototypical member of the family of the aromatic molecules; it exhibits its aromaticity because it meets the requirements of the $(4n+2)$ π electron Hückel rule as a monocyclic and planar polyene containing 6π electrons (isovalent with benzene). The gas-phase isomerization reaction between the cationic forms of tropyl and benzyl ($C_6H_5CH_2$) has been studied extensively in the past.[1–3] The tropyl radical has been suggested to be a possible intermediate in isomerization and ring-opening and closing reactions of the benzyl radical.[2,4] In contrast to the tropylium ion, information on the properties of the tropyl radical is relatively sparse.

Whereas the tropyl cation is more stable than the benzyl cation by 0.24 eV,[5] the benzyl radical is more stable[1] than the tropyl radical by $\sim$0.73 eV. The resonance stabilization for the tropyl radical comes from the resonance energy of the cycloheptatriene system and the delocalization of the unpaired electron present in a degenerate antibonding e_2'' molecular orbital. While the barrier for the isomerization from the tropyl cation to the benzyl cation has been calculated[6] (3 eV), the corresponding value for the neutral species is unknown. However, the tropyl radical is believed to convert rapidly to the benzyl radical.[2,4]

Tropyl has an $\tilde{X}\,^2E_2''$ ground electronic state in D_{7h} symmetry with a dominant electronic configuration of

$$\cdots(a_2'')^2(e_1'')^4(e_2'')^1(e_3'')^0, \tag{1}$$

considering only the π molecular orbitals explicitly. The excitation of one electron forms the excited $\tilde{A}\,^2E_3''$ electronic state with the dominant electronic configuration

$$\cdots(a_2'')^2(e_1'')^4(e_2'')^0(e_3'')^1. \tag{2}$$

Tropyl is the only simple molecular species known with nominal D_{7h} symmetry[2] but is subject to Jahn-Teller distortion from the D_{7h} nuclear geometry in its ground and first excited electronic states, due to their electronic degeneracy. For both the doubly degenerate $\tilde{X}\,^2E_2''$ and $\tilde{A}\,^2E_3''$ states, the Jahn-Teller distortion leads to planar structures with $^2A_2$ and $^2B_1$ symmetries (in the C_{2v} point group). Consequently, the molecule has a very complicated vibronic structure in both its $\tilde{X}$ and $\tilde{A}$ states.

The $\tilde{X}\,^2E_2''$ electronic state of tropyl was previously studied both experimentally and theoretically. Electron spin resonance (ESR) spectroscopy[7] was applied in the early 1960s. Based on the observation of seven equivalent ESR proton hyperfine couplings corresponding to a uniform spin distribution, the effective structure of tropyl was interpreted as corresponding to a dynamic D_{7h} symmetry. Photoelectron spectroscopy[8] presented tropyl as a highly fluxional molecule in its ground electronic state, in agreement with the ESR results. The gas-phase IR absorption spectra of C_7H_7 were recorded in the 400–1800 cm^{-1} spectral energy region.[1] As there was no Jahn-Teller analysis of the observed vibronic structure, no conclusive results about the Jahn-Teller interactions in the $\tilde{X}\,^2E_2''$ electronic state could be produced. *Ab initio* molecular orbital and density functional theory calcu-

---

a)Present address: Laboratory of Molecular Spectroscopy, Institute of Chemistry, Eötvös University, P.O. Box 32, H-1518 Budapest 112, Hungary.

b)Electronic mail: tamiller@chemistry.ohio-state.edu.

lations were also performed on the tropyl radical.[3] Harmonic vibrational frequencies were calculated as well as the first adiabatic and vertical ionization energies. The results indicated that the molecule has a C_{2v} equilibrium geometry.

Thrush and Zwolenik[9] first reported the electronic spectrum of C_7H_7 by direct absorption in the visible region. Another spectroscopic technique applied was [2+1]- and [1+1]-resonance-enhanced multiphoton ionization (REMPI) spectroscopy, performed in the visible[4] and near-UV (Ref. [2]) energy region, respectively. The REMPI work by Pino *et al.*[2] is of central importance here as it provides useful information on the $\widetilde{A}\,^2E_3''$ state vibronic structure.

In the present work, laser-induced fluorescence (LIF) spectroscopy was combined with supersonic free-jet expansion techniques to record the excitation and laser-excited dispersed fluorescence (LEDF) spectra from a number of $\widetilde{A}$-state levels of the tropyl radical for the first time. Consequently, the LIF and REMPI experiments map the $\widetilde{A}$-state vibrational structure and the LEDF experiments map the $\widetilde{X}$ state.

In the preceding paper[10] (Part I), we described the *ab initio* calculations that we have performed with the express purpose of aiding the analysis of the experimentally observed vibronic structure of the tropyl radical in its $\widetilde{X}$ and $\widetilde{A}$ electronic states. In this paper (Part II), we describe first our observation and analysis of the LIF excitation spectrum of the $\widetilde{A}\,^2E_3'' \leftarrow \widetilde{X}\,^2E_2''$ electronic transition of the tropyl radical. We proceed to describe the LEDF spectra from several $\widetilde{A}$-state vibrational levels. The analysis of the LEDF spectra establishes the positions of the $\widetilde{X}$-state vibronic levels. We apply the results of Part I to help assign and analyze the $\widetilde{X}$- and $\widetilde{A}$-state vibronic structures, which consist of both Jahn-Teller active and Jahn-Teller inactive vibrational modes.

The spectroscopic analysis of the $\widetilde{X}$- and $\widetilde{A}$-state vibronic structures of C_7H_7 provides a complete set of Jahn-Teller coupling constants for the linear Jahn-Teller active vibrational modes of each electronic state. It also gives information about their Jahn-Teller distorted potential energy surfaces (PESs) and their Jahn-Teller energy stabilizations. These results are compared to various predictions from *ab initio* calculations of Part I.

The remainder of this paper is organized as follows. In Sec. II, an outline of the theoretical approach that was undertaken to predict the Jahn-Teller distorted vibrational structure is given. It is followed by the experimental details in Sec. III. The experimental results are presented in Sec. IV where the analysis of the spectra takes place. In Sec. V, the experimental Jahn-Teller molecular parameters of the $\widetilde{A}\,^2E_3''$ and $\widetilde{X}\,^2E_2''$ electronic states of C_7H_7 are discussed, compared with the *ab initio* calculated ones, and their values and corresponding ramifications for the Jahn-Teller distorted PES in each case are discussed in relationship to the earlier results for the other quasi-aromatic hydrocarbons, C_5H_5 and $C_6H_6^+$. The paper completes with the conclusions presented in Sec. VI.

II. THEORETICAL

A. Vibronic eigenvalues and eigenfunctions

In Part I, we applied the general theory for Jahn-Teller distortions specifically to the case of C_7H_7. To that treatment, we must add $\hat{\mathcal{H}}_T$, the nuclear kinetic-energy operator, to obtain the complete vibronic Hamiltonian $\hat{\mathcal{H}}$,

$$\hat{\mathcal{H}} = \hat{\mathcal{H}}_T + \hat{V} = \hat{\mathcal{H}}_T + \hat{\mathcal{H}}_h + \hat{\mathcal{H}}_l. \tag{3}$$

Following Part I, the nonzero electronic matrix elements of the terms of the effective potential $\hat{V}$ are given[11] by

$$\begin{aligned}
\langle \Lambda_\pm | \hat{\mathcal{H}}_h | \Lambda_\pm \rangle &= \frac{1}{2}\sum_{i=1}^{p}\sum_{r=+,-}\lambda_i |Q_{i,r}|^2 + \frac{1}{2}\sum_{i=1}^{3N-6-2p}\lambda_i'|Q_i|^2 \\
&= \sum_{i=1}^{p}\sum_{r=+,-}(\sqrt{2}\pi c M_i^{1/2}\omega_{e,i})^2|Q_{i,r}|^2 \\
&\quad + \sum_{i=1}^{3N-6-2p}(\sqrt{2}\pi c M_i^{1/2}\omega_{e,i}')^2|Q_i|^2
\end{aligned} \tag{4}$$

and

$$\langle \Lambda_\pm | \hat{\mathcal{H}}_l | \Lambda_\mp \rangle = \sum_{i=1}^{p} k_i Q_{i,\pm} = \sum_{i=1}^{p}(8\pi^2 c^3 h M_i^2 \omega_{e,i}^3 D_i)^{1/2} Q_{i,\pm}. \tag{5}$$

In this formulation, $\omega_{e,i}$ and $\omega_{e,i}'$ refer to the vibrational frequencies of the ith normal mode, $Q_{i,\pm}$ and Q_i, respectively, defined at the D_{7h} conical intersection X_0 of the $\widetilde{X}$- and $\widetilde{A}$-state PESs of tropyl, and D_i is the linear Jahn-Teller coupling parameter. The sum over i is for the $p=4$ e_3' modes of the $\widetilde{X}\,^2E_2''$ electronic state of C_7H_7 and the $p=3$ e_1' vibrational modes of its $\widetilde{A}\,^2E_3''$ electronic state. As was noted in Part I, the normal coordinates $Q_{i,\pm}$ have been introduced by the relationship

$$Q_{i,\pm} = \rho_i e^{\pm i\phi}. \tag{6}$$

A summary of our calculated PES parameters from Part I is given in Table I.

While in general the potential $\hat{V}$ may be dependent on ϕ, this does not hold for a molecule of nominal D_{7h} symmetry (see Part I). In Part I, we showed that the potential $\hat{V}=\hat{\mathcal{H}}_h+\hat{\mathcal{H}}_l$ has a global minimum for the values of $\rho_i^{\min}$ given by

$$\rho_i^{\min} = \left(\frac{\hbar D_i}{\pi c M_i \omega_{e,i}}\right)^{1/2}, \tag{7}$$

with a Jahn-Teller stabilization energy ε_T (measured with respect to zero at X_0),

$$\varepsilon_T = \sum_{i=1}^{p}\varepsilon_i = \sum_{i=1}^{p}2\hbar\pi c D_i\omega_{e,i}. \tag{8}$$

A high-data throughput computer program called SPEC-SOCJT (Ref. [12]) was specifically designed to obtain the eigenvalues and functions of $\hat{\mathcal{H}}_e$ for the $\widetilde{A}$- and $\widetilde{X}$-state C_7H_7 spectral analysis. It was implemented in FORTAN and C++

TABLE I. Jahn-Teller parameters of the $\tilde{X}\,^2E_2''$ and $\tilde{A}\,^2E_3''$ electronic states of C$_7$H$_7$. [All constants have units of cm^{-1}, except D_i which is unitless (see Part I for details).]

| | $\tilde{X}^2E_2''$ State of C$_7$H$_7$ | | | | | | | $\tilde{A}^2E_3''$ State of C$_7$H$_7$ | | | | | |
| | Calc. | | | Expt. | | | | Calc. | | | Expt. | | |
Mode	ω_i	D_i	ε_i	ω_i	D_i	ε_i	Mode	ω_i	D_i	ε_i	ω_i	D_i	ε_i
15	3356	0.002	7	$\cdots$	$\cdots$	$\cdots$	5	3378	0.004	13	$\cdots$	$\cdots$	$\cdots$
16	1611	0.589	949	1600	0.50	800	6	1641	0.102	167	1519	0.10	152
17	1377	0.295	406	1350	0.12	162	7	1082	1.098	1188	950(10)[a]	0.70	665
18	941	0.013	12	900	0.09	81							
ε_T			1374			1043				1368			817

[a]Anharmonicity constant $\omega_e\chi_e$ in cm^{-1}.

and employed fast computational methods for the construction of the Hamiltonian matrix and the solution of the Schrödinger equation. The data input and output interfaces were developed using MICROSOFT VISUAL C++ tools and allow for a quick exchange of information between the calculational core and the user. The graphic user interface part of the program was developed to display and compare in one step all pairs of $\tilde{X}$- and $\tilde{A}$-state experimental and simulated spectra of the tropyl radical. To facilitate ease of use, the data input can be made in dialog boxes, and the user can also perform a one-dimensional parameter scan with the simple touch of the mouse wheel.

SPEC-SOCJT can be used to numerically solve for the $\tilde{X}\,^2E_2''$ and $\tilde{A}\,^2E_3''$ state vibronic energy levels based on the Hamiltonian matrix defined in Eqs. (4) and (5). Using the known[11] matrix elements of $\hat{\mathcal{H}}$, in terms of the experimental parameters, $\omega_{e,i}$, $\omega'_{e,i}$, and D_i, SPEC-SOCJT can construct this matrix in a suitable basis set and find its eigenpairs. The basis set used in SPEC-SOCJT is a product of electronic and vibrational wave functions represented by

$$|\Lambda\rangle\prod_{i=1}^{p}|v_i l_i\rangle, \qquad (9)$$

with quantum numbers $\Lambda=\pm 1$, $v_i=0,1,2,\ldots$, $l_i=v_i, v_i-2,\ldots,-v_i+2,-v_i$. $\Lambda=\pm 1$ refer to the two electronic components of the doubly degenerate electronic state ($\tilde{X}$ or $\tilde{A}$) of tropyl, v_i are the principal vibrational quantum numbers of the linear Jahn-Teller active vibrational modes, and l_i are their vibrational angular momentum quantum numbers. Since the linear Jahn-Teller term in the Hamiltonian is off-diagonal in the Λ, v_i, and l_i quantum numbers, it is useful to define a quantum number, j, that is conserved and is given by[11]

$$j = l_t + \tfrac{1}{2}\Lambda, \qquad (10)$$

with

$$l_t = \sum_i l_i. \qquad (11)$$

From Eq. (10), it is obvious that there will be multiple energy levels with identical values of j; hence, we define a second quantum number, n_j, which takes on the values $1,2,3,\ldots,\infty$ and serves only to provide unique labels to the

eigenvalues of the same j, ordered by increasing energy. Thus, we denote eigenkets as $|j,n_j\rangle$.

The basis set defined above is infinite in size. Obviously, one must truncate the basis set to some reasonable size before diagonalizing the Hamiltonian matrix. In practice, the calculated eigenvalues were tested for convergence by systematically increasing the number of basis functions until the change in the relevant eigenvalues was less than 1 cm^{-1}. For C$_7$H$_7$, the final matrices used were of order 5×10^4. The size of the blocks in the block-diagonalized Hamiltonian matrix used was of order 7×10^3.

B. Selection rules

The $\tilde{A}\,^2E_3''$-$\tilde{X}\,^2E_2''$ transition is electronically allowed for an electronic transition dipole ($\mu_{x,y}$) perpendicular to the sevenfold axis. Such a dipole will transform as e_1' in D_{7h} symmetry, which we will use to label the observed transitions. The standard vibrational selection rule for an electronic transition in the LIF excitation spectrum from the vibrationless $\tilde{X}$ state is that vibrational progressions are allowed only for totally symmetric (a_1') vibrations, which correspond to ω_1 and ω_2 modes in the $\tilde{A}$ state. In addition, transitions are allowed to even overtones (as they contain an a_1' component) for any vibration, but in a transition where the PES of the two states is not very different, they are expected to be significantly weaker.

These selection rules must be relaxed to take into account the Jahn-Teller effect. The Jahn-Teller effect is expected also to make allowed transitions to the linearly Jahn-Teller active e_1' modes ($\omega_5, \omega_6, \omega_7$) in the $\tilde{A}$ state. However, the j quantum number restricts which Jahn-Teller split components of the e_1' levels that can be accessed. Since the transition selection rule is $\Delta j=0$ and $j=1/2$ for the originating level in the LIF spectrum, transitions can access only $j=1/2$, e_1' Jahn-Teller active components in the $\tilde{A}$ state. Since j is a rigorous quantum number for a linear Jahn-Teller effect and quadratic interactions vanish in the linearly active e_1' mode, we expect $\Delta j=0$ to be a strong selection rule.

In addition, we have to realize that there are linear effects such as Jahn-Teller effects in the e_3' mode of the $\tilde{X}$ state. By similar reasoning, the $\tilde{X}$-state vibronic mixing can there-

fore make allowed transitions to vibrational levels in the $\widetilde{A}$ state involving $j=1/2$, e'_3 modes ($\omega_{15}, \omega_{16}, \omega_{17}, \omega_{18}$).

Quadratic Jahn-Teller interactions while not present in the linearly active modes are present in other modes, specifically e'_2 ($\omega_9, \omega_{10}, \omega_{11}, \omega_{12}$) and $e''_2(\omega_{13}, \omega_{14})$ in the $\widetilde{X}$ state and $e'_3(\omega_{15}, \omega_{16}, \omega_{17}, \omega_{18})$ and $e''_3(\omega_{19}, \omega_{20})$ in the $\widetilde{A}$ state, as shown in Part I. These quadratic interactions might enhance otherwise relatively weak even overtone transitions to these modes. Cross-quadratic interactions can similarly enhance other overtones. The selection rules for these interactions are given in Part I.

For the LEDF transition, very similar considerations apply, but the actual selection and propensity rules depend somewhat upon the $\widetilde{A}$-state level excited. Subsequently, we will analyze LEDF spectra from the $\widetilde{A}$-states levels assigned as 0^0_0, 14^2, and the lowest linear Jahn-Teller active level $|j, n_j\rangle = |1/2, 1\rangle$. Since the pumped levels in the first two cases, 0^0 and 14^2, are totally symmetric, these LEDF spectra should be very similar, varying primarily because of different Franck-Condon factors. From these $\widetilde{A}$-state levels, progressions in a'_1 levels, linearly Jahn-Teller active $j=1/2$, e'_3 levels, e'_1 levels (from $\widetilde{A}$-state Jahn-Teller activity) and overtone bands (possibly enhanced by quadratic Jahn-Teller coupling) should be expected. The same selection rules should hold for the LEDF transitions from the $\widetilde{A}$ state $|1/2, 1\rangle$ level except that one would expect enhanced intensity in the emission to the e'_1 levels in the $\widetilde{X}$ state.

Selection rules resulting from consideration of only the vibronic symmetry of the levels are somewhat more relaxed since they include other, presumably weaker, mechanisms to allow transitions. Generally speaking, the excitation from the vibrationless level of the $\widetilde{X}\,^2E''_2$ state with e''_2 vibronic symmetry will terminate on levels in the $\widetilde{A}\,^2E''_3$ electronic state with e''_3 vibronic for $\mu_{x,y}(e'_1)$ and on e'_2 symmetry for $\mu_z(a''_2)$ and vice versa. We have not specifically invoked these more general selection rules in our assignment of spectral lines; however, there are a number of weak, unassigned lines which may arise from such transitions.

III. EXPERIMENTAL DETAILS

The experimental setup used to obtain both the LIF spectrum of the $\widetilde{A}\,^2E''_3$ electronic state and the LEDF spectra of the $\widetilde{X}\,^2E''_2$ electronic state is depicted graphically in Fig. 1. A few torr of the cycloheptatriene vapor were entrained into the jet flow by passing a carrier gas at a suitable backing pressure over the liquid contained in a stainless steel reservoir maintained at a suitable temperature depending on the vapor pressure. The seeded flow was then expanded through a 300 μm standard pulsed nozzle (General Valve) into the jet chamber which was evacuated by a mechanical booster pump backed by a rotary oil pump. The tropyl radicals were generated *in situ* in the gas pulse of the hydrocarbon precursor mixed with the carrier gas by striking a pulsed electrical discharge. The tropyl radicals were produced by the removal of a hydrogen atom from cycloheptatriene. A summary of the
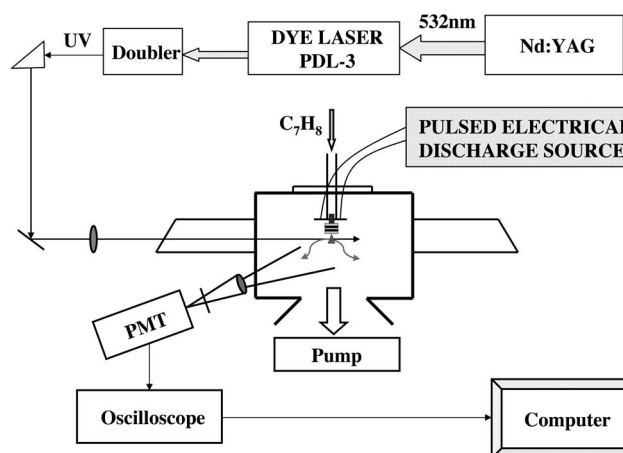

FIG. 1. Schematic diagram of the experimental apparatus for obtaining the LIF spectrum. The apparatus for the LEDF experiments was similar except the fluorescence was dispersed.

experimental conditions for the LIF and LEDF experiments is given in Table II.

The resulting free-jet expansion was crossed approximately 10–15 mm downstream of the pulsed discharge nozzle by the frequency doubled output (Inrad Autotracker II) of a tunable dye laser (SpectraPhysics PDL-3) pumped by the second harmonic of a Nd doped yttrium aluminum garnet (YAG) laser (Quanta Ray DCR) at 532 nm. This work re-

TABLE II. Summary of the conditions used for the LIF and LEDF experiments with the tropyl radical.

Expt.	LIF	LEDF
Carrier gas	He[a]	Ar[b]
Temperature of the sample bomb (°C)	−10	5
Backing pressure (psi)	30–60	30
Opening time of the jet (μsec)	600	300
Discharge voltage (V)	1000	400–500
Discharge pulse duration (μsec)	850	80–200
Resolution (cm^{-1})	4	20
Accumulation time (min)	⋯	90,[c] 60,[d] 30[e]
Slit width (μm)	⋯	125[f]
Grating (grooves/mm)	⋯	1800

[a]The LIF excitation spectrum of tropyl has also been recorded using Ar as a carrier gas and is similar with the one recorded with He.

[b]The LEDF emission spectra collected through bands A–C of the $\widetilde{A}$ state of tropyl (see Fig. 2) have also been recorded using He as a carrier gas and are similar with the ones recorded with Ar. The latter ones are reported since they have a better signal/noise (S/N) ratio.

[c]The accumulation time for the LEDF collection via band A of the $\widetilde{A}$ state of tropyl (see Fig. 2) was extended 2 h for the first 2000 cm^{-1} redshifted from the pumping frequency and 90 min for $>$2000 cm^{-1} above the origin.

[d]The accumulation time for the LEDF collection via band B of the $\widetilde{A}$ state of tropyl (see Fig. 2) was extended to 3 h for the first 2000 cm^{-1} redshifted from the pumping frequency and 60 min for $>$2000 cm^{-1} above the origin.

[e]The accumulation time for the LEDF collection via band C of the $\widetilde{A}$ state of tropyl (see Fig. 2) was extended to 60 min for the first 2000 cm^{-1} redshifted from the pumping frequency and 30 min for $>$2000 cm^{-1} above the origin.

[f]The fluorescence emission from bands A to C of the $\widetilde{A}$ state of tropyl (see Fig. 2) was also dispersed using an entrance slit width of 375 μm before the monochromator, with a corresponding S/N approximately three times as much larger compared to the one with 125 μm. The vibronic structure observed in both cases is consistent.
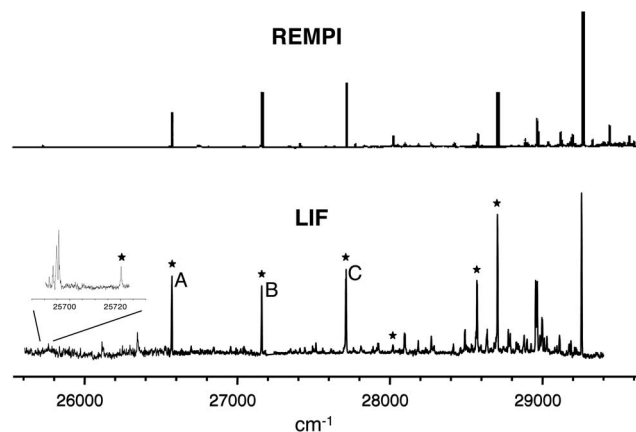
REMPI

LIF

FIG. 2. REMPI (top) and LIF (bottom) spectra of C_7H_7. The REMPI spectrum was taken from Ref. 2 and the LIF spectrum comes from the present work. The stars in the excitation spectrum designate the bands of the $\tilde{A}$ electronic state from which we have dispersed the emission. Of central importance for the analysis of the vibronic structure of the $\tilde{X}\,^2E_2''$ electronic state is the LEDF emission collected by pumping bands A–C of the $\tilde{A}\,^2E_3''$ electronic state. The x axis indicates the excitation frequency. The intensities observed in the LIF spectrum were not corrected for the dye-laser power deviations. The experimental resolution was 4 cm^{-1}, limited by the unresolved rotational contour of the vibronic bands.

quired the use of four laser dyes, namely, LDS 698, 750, 751, and 765. The delay time between the striking of the discharge and the firing of the dye laser, along with the time delay and the opening time of the nozzle, were controlled by a pulse generator (Stanford Research DG535).

The probe beam passed through the vacuum chamber. The fluorescence signal was collected perpendicularly to the laser beam. On one side of the chamber, the fluorescence emission was collimated by a 2.5 cm diameter lens ($f/1$) and a second lens focused the radiation onto the photocathode of the photomultiplier tube (EMI 9659Q) connected to an amplifier. The amplified LIF signal was integrated by a boxcar averager, digitized by an analog-to-digital converter and fed into a personal computer for further data processing. On the other side of the chamber, the fluorescence emission was dispersed by a Spectra Pro 300i monochromator using a 1800 groove/mm grating and then imaged onto an intensified charge-coupled device (ICCD). The detection of the dispersed photons was done with the Princeton Instruments PI-MAX512HB camera. The entrance slit width of the monochromator was set at 125 μm. The emission frequencies reported for the LEDF spectra and the excitation frequencies for the LIF spectrum of the tropyl radical were obtained by calibrating them against a Fe–Ne optogalvanic lamp and known Ar atomic lines.

IV. RESULTS

A. Assignment of the $\tilde{A}\,^2E_3''$ electronic state

Although the REMPI spectrum of "cold" C_7H_7 has been known[2] for some time, there are still questions as to the complete assignment of its spectrum. For this work, we have recorded the LIF spectrum of the $\tilde{A}\,^2E_3''$-$\tilde{X}\,^2E_2''$ electronic transition of C_7H_7. The LIF and REMPI spectra of C_7H_7 are shown in Fig. 2. The stars on the LIF spectrum designate the

TABLE III. Frequencies and $\tilde{A}\,^2E_3''\leftarrow\tilde{X}\,^2E_2''$ LIF excitation assignments of C_7H_7.

	Frequency (cm^{-1})			
	Ref. 2		This work	
Assignment[a]	Absolute	Relative to 0_0^0	Absolute	Relative to 0_0^0
···	25 719[b]	···	25 719[b]	−853
···	···	···	26 117[c]	−455
···	···	···	26 345[c]	−227
$\lvert\frac{1}{2},1\rangle$ (A)	26 573[b]	0	26 572[b]	0
(14_0^2)[d] (B)	27 159	586	27 160	588
$\lvert\frac{1}{2},2\rangle$ (C)	27 711	1138	27 713	1141
···	···	···	27 926[c]	1354
$(2_0^1 14_0^2)$[d] (α)	28 018	1445	28 018	1446
$\lvert\frac{1}{2},3\rangle$	···	···	28 096	1524
···	···	···	28 185[c]	1613
(8_0^2)	28 269	1696	28 271[e]	1699
···	···	···	28 415[c]	1843
$\lvert\frac{1}{2},4\rangle$	···	···	28 493	1921
$18_0^1 \lvert\frac{1}{2},2\rangle$ (β)	28 571	1998	28 570	1998
13_0^2	···	···	28 636[e]	2064
$(16_0^1 14_0^2)$[d] (γ)	28 704	2131	28 705	2133
19_0^2	···	···	28 780[e]	2208
···	···	···	28 833[c]	2261
$(2_0^2 14_0^2)$[d] (δ)	28 877	2304	28 876	2304
···	···	···	28 898[c]	2326
···	···	···	28 925[c]	2353
11_0^2	28 954	2381	28 955	2383
$17_0^1 \lvert\frac{1}{2},2\rangle$ (ε)	28 965	2392	28 966	2394
···	···	···	28 997[c]	2425
···	···	···	29 029[c]	2457
$\lvert\frac{1}{2},5\rangle$	29 110	2537	29 111	2539
$4_0^2 17_0^1$ (ζ)	29 184	2611	29 180	2608
···	···	···	29 210[c]	2638
$16_0^1 \lvert\frac{1}{2},2\rangle$ (η)	29 254	2681	29 256	2684

[a]We denote with letters (A–C) those bands of the $\tilde{A}$ electronic state from which we analyze the emission spectra. In the first column under assignment, we give the spectroscopic designation of the terminating energy levels of the transitions originating in $\lvert\frac{1}{2},1\rangle$ of the $\tilde{X}$ electronic state of C_7H_7. The Greek letters denote other assigned transitions that do not terminate in Jahn-Teller active e_1' vibrational levels of the $\tilde{A}$ state.

[b]In Ref. 2, the electronic origin of the $\tilde{A}\,^2E_3''\leftarrow\tilde{X}\,^2E_2''$ electronic spectrum of C_7H_7 was tentatively (Ref. 13) assigned to the weak band at $25\,719\pm3$ cm^{-1}. We have reassigned it to the feature at 26 573 cm^{-1} (band A) and the relative to 0_0^0 excitation frequencies, which are given in the third column of the table, follow our reassignment.

[c]Possibly due to artifacts of the discharge.

[d]The vibronic-band profiles of α, γ, and δ resemble that of band's B as well as show similar quadratic Jahn-Teller splittings to those observed in band B.

[e]Tentative assignment.

bands of the $\tilde{A}$ electronic state of tropyl from which we have dispersed the emission. As many laser dyes were used in the LIF and REMPI experiments, the relative intensities in the spectra only have a qualitative value. The first column of Table III lists the transition from the vibrationless level of the $\tilde{X}$ state to the assigned terminating $\tilde{A}$-state vibrational level in the LIF spectrum using D_{7h} notation, while the second and third columns of Table III give the experimental frequency, absolute and relative to the origin, from the REMPI experiment.[2] The fourth and fifth columns of the same table

list the corresponding frequencies that were recorded in the LIF experiment. There is general agreement between the measured frequencies in the LIF work and the results from the REMPI experiment, as one can see from Fig. 2 and Table III. As Ref. 2 persuasively argues that the REMPI spectrum is solely the tropyl isomer of C_7H_7, it follows that the LIF spectrum must be the same.

Our spectral assignments of most of the observed lines in the LIF spectrum are guided by our theoretical calculations from Part I of the $\tilde{A}\,^2E_3''$ state. However, we assigned the electronic origin of the $\tilde{A}\,^2E_3''$-$\tilde{X}\,^2E_2''$ excitation spectrum at $26\,572 \pm 4$ cm^{-1}, hereafter referred to as band A, primarily based on experimental observations. Note this is a reassignment for the electronic origin of the $\tilde{A}\,^2E_3'' \leftarrow \tilde{X}\,^2E_2''$ REMPI spectrum of the tropyl radical and that Table III reflects this change.

Although we did not perform detailed fluorescence-lifetime measurements on C_7H_7, we observed that band A was the lowest-frequency band, in this energy region, that showed a total fluorescence temporal profile consistent with the one "expected" for tropyl. Specifically, we noticed that the temporal profile for bands A–C of the $\tilde{A}$ electronic state had lifetime of approximately 2 μs and that it reduced to 1.1 μs for the three bands in the higher energy region from which we recorded the emission (see Fig. 2). In the energy region lower than 26 572 cm^{-1}, the three bands at 25 719, 26 117, and 26 345 cm^{-1} showed a temporal profile with lifetime $\lesssim$500 ns (see Table III). The feature at 25 719 cm^{-1}, which was previously assigned by Pino *et al.*[2] as the origin of the $\tilde{A} \leftarrow \tilde{X}$ electronic spectrum of the tropyl radical, likely corresponds to a hot band; it was always weak but not always reproducible in the recorded REMPI spectra.[13]

However, a few words should be said about comparing calculated and observed frequencies. Indeed, in Table VII of Part I, three calculations for the cation are listed. For the neutral radical, there are four calculations, one (B3LYP) constrained to a D_{7h} geometry for the $\tilde{X}$ state and two more (B3LYP and CASSCF) at the global minimum of the PES, plus one (CASSCF) for the $\tilde{A}$ state at its global minimum. All the calculations for the neutral yield two frequencies, one each for the $^2B_1$ and $^2A_2$ symmetries. It is clear that for linearly Jahn-Teller active modes, unperturbed frequencies at D_{7h} symmetry are required. The frequencies and the normal coordinates are consistently obtained with the RHF/6-31G** calculation for the ground state cation while the distortion vectors are derived from the EOMEA-CCSD/TZ2P calculation for the neutral $\tilde{X}$ and $\tilde{A}$ states. Hence, for the Jahn-Teller active modes, we refer to the frequencies from the RHF calculation of the cation at D_{7h} symmetry, as are listed in Table I.

For the linearly non-Jahn-Teller frequencies such as ω_{14}, this consideration does not apply. However, using calculated frequencies at D_{7h} symmetry is likely the right physical choice and certainly avoids the problem of mixing mode numbering for D_{7h} and C_{2v} symmetry. In discussing our assignments, we shall reference as appropriate the calculated B3LYP calculations for the D_{7h} cation because in the radical,
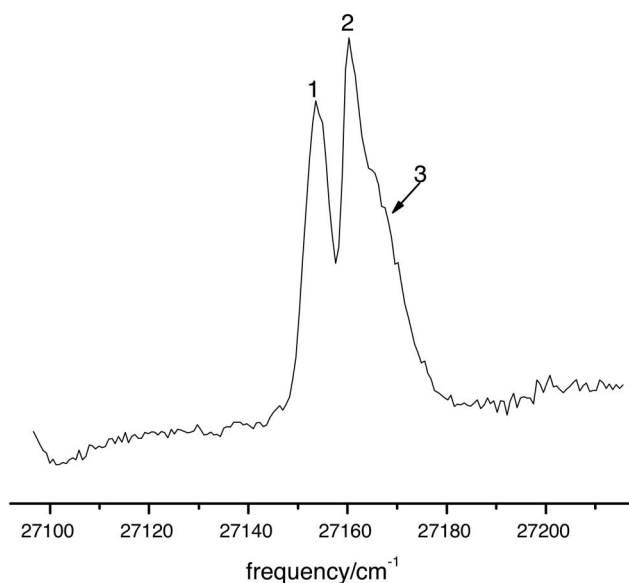

FIG. 3. Expanded view of band B of Fig. 1 with three components of bands indicated. This spectrum was taken at high laser power to maximize S/N. With the power lowered to avoid any broadening, peak 3 is more resolved and pronounced.

the extra electron occupies a weakly bonding orbital both in the $\tilde{X}$ and $\tilde{A}$ states. We think that these are probably the most reliable, but note that reference to Table VII of Part I shows that no outstanding differences exist among the various D_{7h} calculations of the frequencies.

The second intense feature, labeled band B in Fig. 2, in the LIF excitation spectrum appears at 27 160 cm^{-1}, 588 cm^{-1} above the origin. The assignment of this band is nontrivial. From Table VII of Part I, this is a much lower frequency than that of any totally symmetric fundamental. Based on the $\tilde{A}\,^2E_3''$ state calculated Jahn-Teller parameters, it is likewise too low a frequency for the lowest e_1' Jahn-Teller active level, $|1/2, 1\rangle$. A similar conclusion is reached for the e_3' levels, allowed by Jahn-Teller activity in the $\tilde{X}$ state, for which the lowest-frequency mode is ω_{18} which is predicted near 900 cm^{-1}. This leaves even overtones as the only possibility. 14^2 seems the most likely assignment based on the calculated frequency of $(2 \times 224) = 448$ cm^{-1}.

This assignment is strengthened by the fact that the analysis in Part I predicted that the vibrational mode $\omega_{14}(e_2'')$ is characterized by a large cross-quadratic Jahn-Teller coupling constant in the $\tilde{A}$ electronic state. The quadratic Jahn-Teller effect will split the first overtone of $\omega_{14}(e_2'')$ in the $\tilde{A}$ state into four levels with transitions from the vibrationless $\tilde{X}$ state allowed to three. There is experimental evidence of a splitting [smaller than but similar to the ones observed in the ground state vibronic structure of $C_6H_6^+$ (Ref. 14)] of the first overtone of ω_{14} in the $\tilde{A}$ electronic state of tropyl. Figure 3 shows three features in band B with observed spectral line positions at $\approx$27 158, 27 160, and 27 162 cm^{-1}. We have dispersed the emission from all three features and found them to be similar.

This assignment places the fundamental of ω_{14} in the $\tilde{A}$ state at 294 cm^{-1} neglecting anharmonicity, although there
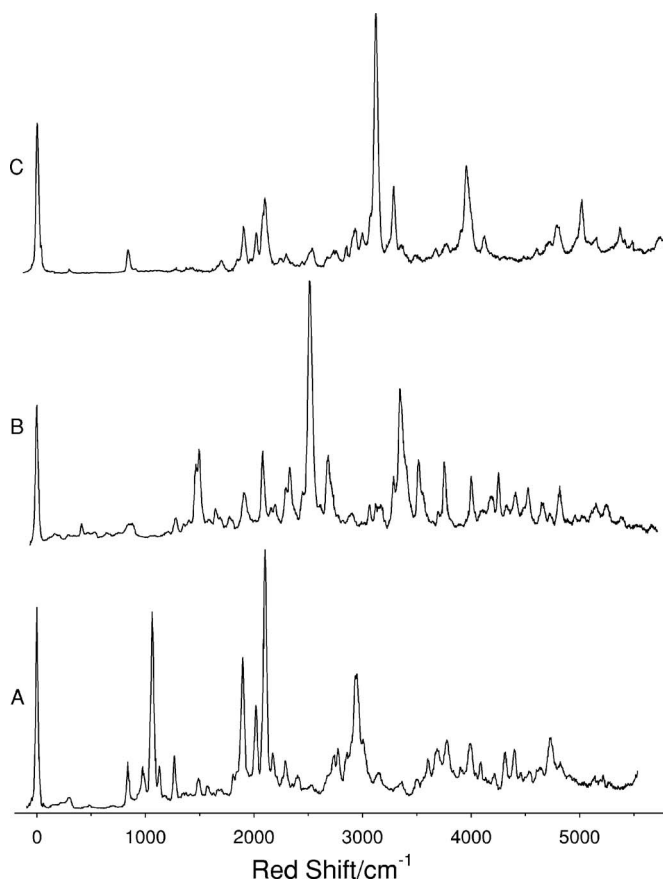
FIG. 4. Dispersed fluorescence spectra of the C_7H_7 radical collected by pumping bands A (bottom), B (middle), and C (top) of the $\tilde{A}\,^2E_3''$ electronic state. The entrance slit width before the monochromator was 125 μm. The x axis indicates (red)shift from the pump frequency. The intensities were not corrected for the grating efficiency and the camera sensitivity curves. The experimental resolution was 20 cm^{-1}. Note also that the structure observed approximately $<$700 cm^{-1} in the emission from bands A and B is due to artifacts of the discharge source.
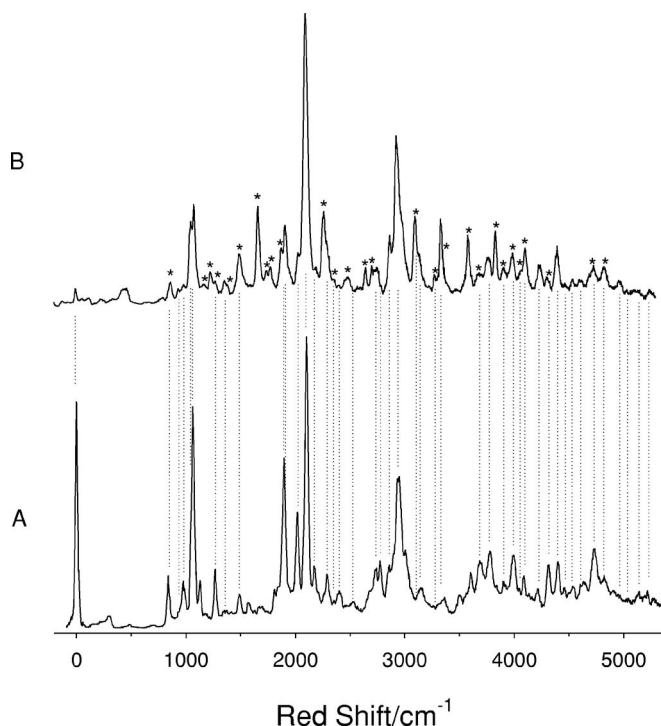

FIG. 5. Dispersed fluorescence spectra of the C_7H_7 radical collected by pumping bands A (bottom) and B (top) of the $\tilde{A}\,^2E_3''$ electronic state. For the emission from band A, the x axis indicates (red)shift from the pump frequency. The emission through band B in this figure corresponds to the subtraction of 415 cm^{-1} from the emission frequencies of Fig. 4(B). The intensities were not corrected for the grating efficiency and the camera sensitivity curves. The experimental resolution was 20 cm^{-1}.

may be substantial contributions from anharmonicity, especially given the low frequency of this vibration. We examined the emission spectra from bands A and B shown in the bottom and middle traces of Fig. 4, respectively. Based on the above assignment for band B, we expect that its emission to the $\tilde{X}$ electronic state will be allowed only in double quanta, i.e., $\Delta\omega=0, \pm 2, \pm 4, \ldots$. By subtracting 415 cm^{-1} from the emission frequencies observed in the LEDF spectrum of Fig. 4(B), we are led to the spectrum of Fig. 5(B) which seems to be almost identical with the emission from band A, shown in Figs. 4(A) and 5(A). The correspondence between the spectra of Figs. 5(A) and 5(B) is depicted by dotted lines. We conclude that the predominant mechanism of emission from band B is for $\Delta\omega=0$, which corresponds to the transition to the level 14_2 of the $\tilde{X}$ state, with a fundamental of ω_{14} in the $\tilde{X}$ state at 208 cm^{-1}, neglecting anharmonicity. By comparing the spectra of Figs. 4(A) and 4(B), we find a common set of experimental frequencies. For the emission from band B, corresponding transitions to the $\tilde{X}$ state with $\Delta\omega=-2$ are identified by stars Fig. 5(B).

The next intense feature (band C in Fig. 2) to the blue in the LIF spectrum peaks at 27 713 cm^{-1}, 1141 cm^{-1} above the

origin. The $\tilde{A}\,^2E_3''$ state theoretically calculated Jahn-Teller parameters lead to a simulation with an intense feature lying in the energy region of band C. The only other allowed transition expected in this region is again an overtone, 20_0^2, predicted at 1128 cm^{-1} neglecting anharmonicity. As the vibrational frequency analysis of Part I predicts a small quadratic Jahn-Teller coupling constant for $\omega_{20}(e_3'')$ in the $\tilde{A}$ state, we favor the assignment of this band to a transition to a Jahn-Teller level $|1/2,2\rangle$.

We assign the weak peak at 28 018 cm^{-1}, 1446 cm^{-1} above the origin, to the allowed transition $2_0^1 14_0^2$. Additionally, the emission through this band, notwithstanding its broadness, resembles the emission through band B. The experimental frequency of the fundamental of ω_2 is therefore determined to be 858 cm^{-1} which compares well with the theoretical value of 881 cm^{-1}. We probably do not observe the transition to the level 2^1 of the $\tilde{A}$ electronic state due to a weak Franck-Condon factor. Note that this vibration was previously observed in electronic transitions to Rydberg states[4] of C_7H_7 with frequency at 862 $\pm$ 6 cm^{-1}, as well as in the $\tilde{X}\,^1A_1'$ state[15] of $C_7H_7^+$ with frequency at 868 cm^{-1}.

The first prominent feature in the higher energy region of the LIF spectrum appears at 28 570 cm^{-1}, 1998 cm^{-1} above the origin. Based on the theoretically calculated frequencies, possible transitions for assignment to this experimental feature are the overtones 19_0^2, 13_0^2, and 18_0^2, predicted, neglecting anharmonicity, at 2158, 2122, and 1796 cm^{-1}, respectively. The transition to the combination between band C and the

fundamental of $\omega_{18}(e'_3)$, assuming that the experimental frequency for the latter is 857 cm^{-1}, is also a possibility. As mode ω_{13} is not quadratically active in the $\widetilde{A}$ state, the strongest candidates for assignment are either 18_0^2, 19_0^2 or the transition to the combination of $|1/2,2\rangle$ and ω_{18}. We favor the assignment of the feature at 28 570 cm^{-1} to the transition to the combination between band C and the fundamental of ω_{18}, as this mode is linearly Jahn-Teller active in the $\widetilde{X}\ ^2E''_2$ electronic state. We do not observe a transition to the fundamental of ω_{18} of the $\widetilde{A}$ state possibly due to poor Franck-Condon factors. As we will see later in the analysis, transitions to the fundamentals of $\omega_{16}(e'_3)$ and $\omega_{17}(e'_3)$ are also not observed experimentally. Transitions to their combination levels with bands B and C may be assigned. The emission spectrum collected through this band, notwithstanding its broadness, is consistent with this assignment.

The next intense feature peaks at 28 705 cm^{-1}, 2133 cm^{-1} above the origin. This is assigned as a transition to a combination between band B and the fundamental of $\omega_{16}(e'_3)$, which is Jahn-Teller active in the $\widetilde{X}$ state, assuming that the experimental frequency for the latter is 1545 cm^{-1}, with a theoretical value of 1568 cm^{-1}. The following reasoning also supports the above assignment. We examined the intensity profile of this feature in the $\widetilde{A}$ state, as well as that of the feature peaking at 29 256 cm^{-1} which as we will see is also assigned as a transition to a combination level of the fundamental of ω_{16} with band C. As their relative intensities compare well with those of bands B and C and considering also that the linear Jahn-Teller constant of ω_{16} has been theoretically predicted to be the largest in the $\widetilde{X}\ ^2E''_2$ electronic state, we feel that the above assignment is the most reasonable one in light of the experimentally observed line intensities. Finally, we note that the emission spectrum through this band, notwithstanding its broadness, is consistent with this assignment.

The weak feature at 28 876 cm^{-1}, 2304 cm^{-1} above the origin, may be assigned to the transition $2_0^2 14_0^2$. There is no other reasonable candidate based on the theoretically calculated frequencies. This assignment presupposes no anharmonicity in the $\widetilde{A}$-state potential of the ring-breathing mode ω_2. The intense feature at 28 955 cm^{-1}, 2383 cm^{-1} above the origin, may be assigned to the transition 11_0^2 which is predicted at 2510 cm^{-1}, neglecting anharmonicity and based on the theoretically calculated frequency of $\omega_{11}(e'_2)$. This transition may be gaining intensity in the $\widetilde{A}$ state due to an intensity-borrowing mechanism that involves the band centered at 28 966 cm^{-1}. We assign the intense feature at 28 966 cm^{-1} (2394 cm^{-1} above the origin) as the transition to the combination between band C and the fundamental of $\omega_{17}(e'_3)$. This assignment is based on the good match between the theoretically calculated frequency of ω_{17} at 1313 cm^{-1} and the experimentally determined value of 1253 cm^{-1}. No other plausible candidate could be found. The weak feature at 29 180 cm^{-1}, 2608 cm^{-1} above the origin, may be assigned to the transition $4_0^2 17_0^1$, following the same methodology of assignment. The experimental frequency, neglecting anharmonicity, of the fundamental of ω_4 is 677 cm^{-1} and is in

good agreement with the theoretically calculated frequency of 664 cm^{-1}. Finally, the strongest feature in the high energy region at 29 256 cm^{-1}, 2684 cm^{-1} above the origin, is assigned to the transition to the combination band between band C and the fundamental of $\omega_{16}(e'_3)$.

Several other tentative assignments to weak experimental features were made, namely, to the bands peaking at 28 271, 28 636, and 28 780 cm^{-1}. These bands were assigned, based on the theoretical expectations from the calculated frequencies and by a process of elimination, to 8_0^2, 13_0^2, and 19_0^2, respectively. A number of weak bands have appeared in our LIF spectrum and not in the REMPI spectrum. These features are likely due to artifacts of our discharge source. As it has previously been discussed,[16] molecules may fragment and/or isomerize before emission and it is difficult to distinguish among them without the mass discrimination of the REMPI experiment.

Our assignments for the $\widetilde{A}$-state levels $\leqslant$2700 cm^{-1} are in disagreement with the past work,[2] as the origin of the $\widetilde{A}\ ^2E''_3$-$\widetilde{X}\ ^2E''_2$ excitation spectrum was tentatively[13] assigned to the weak feature at 25 719 cm^{-1}, whereas we assign it to the band at 26 572 cm^{-1}. Additionally, Pino *et al.*[2] did not attempt a multimode Jahn-Teller analysis as we did in the present work, owing to the fact that they identified only a small number of lines in the $\widetilde{A}\ ^2E''_3$ electronic state and hence could not provide reliable experimental Jahn-Teller parameters for the excited electronic state. Their theoretical calculations did not involve computation of the $\widetilde{A}$-state linear Jahn-Teller parameters.

We simulated the vibronic structure of the $\widetilde{A}\ ^2E''_3$-$\widetilde{X}\ ^2E''_2$ excitation spectrum, using the above assignments, assuming that only the vibrationless level of the $\widetilde{X}$ electronic state, i.e., $|\frac{1}{2},1\rangle$, is populated in the jet expansion. The experimental LIF spectrum of the $\widetilde{A}\ ^2E''_3$ state of tropyl is shown in Fig. 6(A). The assignment of the transitions to the $j=1/2$ Jahn-Teller vibronic levels started with a simulation of the spectrum using the theoretically calculated Jahn-Teller parameters of the $\widetilde{A}\ ^2E''_3$ state, listed in the ninth and tenth columns of Table I [Fig. 6(B)]. Note that only modes ω_6 and ω_7 were introduced in the Jahn-Teller simulation of the $\widetilde{A}$ electronic state. The excitation intensities are calculated by SPEC-SOCJT, assuming that all the oscillator strength results from the Jahn-Teller mixing for the e'_1 modes of the $\widetilde{A}$ state. The most intense feature to the blue of the origin of the simulation in Fig. 6(B) must reasonably correlate with band C of the experimental spectrum. This assignment produces an $\widetilde{X}$-state simulation consistent with the experimental LEDF observations of the ground electronic state structure, as we will describe in Sec. IV B 2. The transitions to the next three members of the $j=\frac{1}{2}$ vibronic progression were tentatively assigned to weak features of the spectrum by a process of elimination, and the Jahn-Teller parameters were adjusted accordingly [see Fig. 6(C)]. Specifically, the band at 28 096 cm^{-1} may be attributed to the transition to $|\frac{1}{2},3\rangle$, the band at 28 493 cm^{-1} to the transition to $|\frac{1}{2},4\rangle$, and the transition to the level $|\frac{1}{2},5\rangle$ may be assigned to the feature at 29 111 cm^{-1}. The 12th and 13th columns of Table I summa-
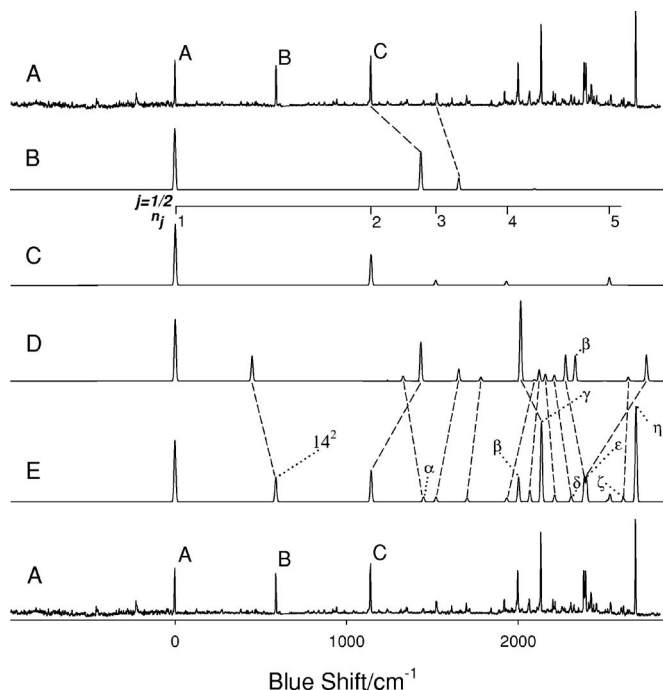
FIG. 6. Excitation spectrum of C_7H_7, laser excited from the vibrationless level of the $\tilde{X}\,^2E_2''$ electronic state. (A) Experimental trace. Bands A–C are denoted in the figure (top and bottom traces). (B) Positions of the transitions to the e_1' Jahn-Teller active levels with $j=\frac{1}{2}$ symmetry, computed using the theoretically calculated Jahn-Teller parameters of the $\tilde{A}\,^2E_3''$ electronic state. (C) Same as (B) but using the best-fit Jahn-Teller parameters of the $\tilde{A}\,^2E_3''$ electronic state. (The first five members of the $j=\frac{1}{2}$ progression are shown.) (D) Same as (B) plus the positions of the transitions to the first overtones of ω_{19}, ω_8, ω_{14}, ω_{13}, and ω_{11} as well as a number of combination levels (labeled in E as α, β, γ, δ, ε, and ζ). The transition to the combination level η (labeled in E) is not shown in (D) since it is not predicted within the energy range of this spectrum. The intensities of the transitions to the levels $\omega_{19}^2 - \omega_{11}^2$ and $\alpha - \eta$ were adjusted to the experimentally observed. (E) Same as (D) but using the experimentally determined spectral parameters of the $\tilde{A}\,^2E_3''$ electronic state.

rize the experimental Jahn-Teller parameters of the $\tilde{A}\,^2E_3''$ electronic state. The "comb" in Fig. 6(C) marks the progression in the $j=\frac{1}{2}$ levels. Only the first five members are shown. Table IV summarizes the calculated and experimentally observed Jahn-Teller transitions. Notice the good agreement between the theoretically calculated frequencies and the experimentally recorded ones.

TABLE IV. Calculated and experimentally observed Jahn-Teller transitions to the $\tilde{A}\,^2E_3''$ electronic state of C_7H_7. (In the first column, we give the spectroscopic designation of the vibronic terminating levels of the transitions to the $\tilde{A}\,^2E_3''$ electronic state originating in $|\frac{1}{2},1\rangle$ of the $\tilde{X}\,^2E_2''$ electronic state of C_7H_7. We follow the $|j,n_j\rangle$ formalism. The calculated excitation frequencies were based on the best-fit Jahn-Teller parameters of the $\tilde{A}\,^2E_3''$ electronic state and are given in the second column, while their experimental counterparts are listed in the third column.)

$\begin{array}{c}\lvert\frac{1}{2},n_j\rangle\\ n_j\end{array}$	Calc.	Expt.
1	0	0
2	1141	1141
3	1518	1524
4	1929	1921
5	2529	2539

Figure 6(D) presents the transitions to the $j=1/2$ levels of the $\tilde{A}$ state plus all other transitions that we previously assigned, i.e., those terminating in the levels 14^2, 8^2, 13^2, 19^2, and 11^2, as well as those in the combinations $2^1 14^2$ (α), $18^1|\frac{1}{2},2\rangle$ (β), $16^1 14^2$ (γ), $2^2 14^2$ (δ), $17^1|\frac{1}{2},2\rangle$ (ε), $4^2 17^1$ (ζ), and $16^1|\frac{1}{2},2\rangle$ (η). The spectrum of Fig. 6(D) was calculated based on the theoretically determined spectral parameters of the $\tilde{A}\,^2E_3''$ electronic state. The intensities of the transitions were matched to those of the experimental spectrum. With further adjustment of their position to the experiment, we are led to Fig. 6(E) which is the same as Fig. 6(D) but calculated based on the experimental spectral parameters of the $\tilde{A}\,^2E_3''$ electronic state.

B. Assignment of the $\tilde{X}\,^2E_2''$ electronic state

LEDF spectra were collected from all the starred bands of Fig. 2. Detailed analysis was performed upon each of the three bands labeled A, B, and C in the C_7H_7 excitation spectrum shown in Fig. 2. The data from the other starred bands were largely redundant and of inferior quality due to lower signal/noise and/or additional spectral broadening and congestion. The $\tilde{A}\,^2E_3''$ state assignments are critical to the interpretation of the LEDF spectra. Our initial assignments for the emission frequencies, including particularly consideration of intensities, were largely based on our *ab initio* spectral parameters for the ground electronic state. A summary of all emission frequencies lower than 3000 cm^{-1}, as well as a number of emission frequencies of the higher energy region, originating from bands A to C of the $\tilde{A}$ electronic state is given in Table V. The emission frequencies listed in the second and fifth columns arise from the emission from bands A and C, respectively. The emission frequencies in the third column were produced by subtracting 415 cm^{-1} from the ones observed in the emission from band B in accordance with $\Delta v = 0$, with the data from the starred bands listed in the fourth column of the table ($\Delta v = -2$). The average value of the observed emission frequencies from bands A to C of the $\tilde{A}$ electronic state is given in the sixth column.

1. Emission from bands A and B of the $\tilde{A}$ electronic state of C_7H_7

The vibronic structure of the emission spectra from bands A to C of the $\tilde{A}$ state was considered simultaneously during the process of assignment; however, it is easier to discuss bands A and B first since they contain much redundant information, and then discuss band C. We first make assignments to transitions to the e_3' Jahn-Teller vibronic levels and then consider the transitions to a number of other vibrational levels as well as their combinations with the e_3' Jahn-Teller levels. The experimental LEDF spectrum from band A of the $\tilde{A}\,^2E_3''$ electronic state is shown in Fig. 7(A). Predicted transitions involving the Jahn-Teller active levels $|1/2, n_j\rangle$ are shown in Figs. 7(B)–7(G). The emission intensities are calculated by SPEC-SOCJT, assuming that all oscillator strength results from the Jahn-Teller mixing for the e_3' vibrational modes in the $\tilde{X}\,^2E_2''$ state and the e_1' vibrational

TABLE V. Experimentally observed spectral transitions to the $\tilde{X}\,^2E_2''$ electronic state originating in bands A–C of the $\tilde{A}\,^2E_3''$ electronic state of C_7H_7. [In the first column, we give the spectroscopic designation of the terminating $\tilde{X}$ state vibrational energy levels of the transitions originating in bands A–C of the $\tilde{A}$ electronic state. The corresponding experimental emission frequencies, in cm^{-1}, are given in the second to fifth columns and their average, in cm^{-1}, in the sixth column of the table. As the emission from band B to the $\tilde{X}$ electronic state is allowed only in double quanta, i.e., $\Delta\omega=0$ (third column) and $\Delta\omega=-2$ (fourth column), the emission frequencies presented in the third column were produced by subtracting (by 415 cm^{-1}) the ones observed in the LEDF experiment listed in the fourth column of the table (see also Sec. IV A for details). Assignments to all experimental bands lower than 3000 cm^{-1} are presented as well as an additional number of bands of the higher energy region.]

| | | Emitting State[a] | | | |
| | | Band B | | | |
Assignment ($\lvert j,n_j\rangle$)	Band A	$\Delta v = 0$	$\Delta v = -2$	Band C	Average
$\lvert \frac{1}{2},1\rangle$	0	0[b]	0	0	0
2_1	838	842[c]	u	840	840
$\lvert \frac{1}{2},2\rangle$	927[c]	926	$\cdots$	924	926
12_2	974	976	$\cdots$	$\cdots$	975
$7_1{}^d$	1059	1061	$\cdots$	$\cdots$	1060
20_2	1128	$\cdots$	$\cdots$	$\cdots$	1128
4_2	1261	1263	1267	1267	1264
$\lvert \frac{1}{2},3\rangle$	1374	u	u	1379	1376
$6_1{}^e$	1482	1482	u	$\cdots$	1482
$8_2{}^f$	1577	$\cdots$	1578	$\cdots$	1577
$\lvert \frac{1}{2},4\rangle$	1617	u	u	$\cdots$	1617
2_2	1678	u	1680	1682	1680
2_1+12_2	1807	u	1806	u	1806
$\lvert \frac{1}{2},5\rangle$	1893	u	u	1895	1894
2_1+7_1	$u\,(\eta)$	1900	1900	$u\,(\beta)$	1900
$\lvert \frac{1}{2},6\rangle$	2013	2013[c]	$\cdots$	2014	2013
$19_2{}^g$	u	u	2081	2081[c]	2081
$7_2{}^d$	2100	2100	u	2099	2100
$\lvert \frac{1}{2},7\rangle$	u	u	2146	u	2146
7_1+20_2	2180	2182	2190	$\cdots$	2184
$4_2+12_2{}^g$	u^c	u	$\cdots$	2242	2242
$13_2{}^g$	2288	u^c	2288	2288	2288
4_2+7_1	u^c	u	u	$\cdots$	$\cdots$
$\lvert \frac{1}{2},8\rangle$	2340	2340	u	2340[c]	2340
$6_1+\lvert \frac{1}{2},2\rangle^e$	2408	2408	u^c	$\cdots$	2408
$\lvert \frac{1}{2},9\rangle$	$\cdots$	$\cdots$	$\cdots$	$\cdots$	$\cdots$
11_2	2529	u^c	u	2531	2530
$\lvert \frac{1}{2},10\rangle^f$	2529	u^c	u	2531	2530
$2_2+12_2{}^g$	u	2652	u	2657	2654
$2_2+7_1{}^h$	2737 (θ)	2739	u	2741 (γ)	2739
$\lvert \frac{1}{2},11\rangle$	2787	u^c	2787	2784	2786
$2_1+\lvert \frac{1}{2},6\rangle$	2852[c]	2856[c]	u	2849	2852
2_1+7_2	2940 (ι)	2938	$\cdots$	2942 (δ)	2940
$7_1+\lvert \frac{1}{2},5\rangle$	2953 (α)	u	$\cdots$	$\cdots$	2953
$7_1+\lvert \frac{1}{2},6\rangle$	$u\,(\beta)$	u	3070	$\cdots$	3070
$7_3{}^f$	u	u	3122	3122	3122
$7_1+\lvert \frac{1}{2},7\rangle$	$u\,(\gamma)$	u	u	$\cdots$	$\cdots$
10_2	$\cdots$	3287	3286	3287	3287
2_2+7_2	3778 (κ)	3778	u	3778 (ε)	3778
2_1+7_3	$\cdots$	$\cdots$	$\cdots$	3962 (ζ)	3962
$7_2+\lvert \frac{1}{2},5\rangle$	3993 (δ)	3993	3995	u	3994
$7_2+\lvert \frac{1}{2},6\rangle$	4097 (ε)	4097	4097	u	4097
7_4	$\cdots$	$\cdots$	$\cdots$	4125	4125
$7_2+\lvert \frac{1}{2},7\rangle$	4233 (ζ)	u	$\cdots$	$\cdots$	4233

TABLE V.   (*Continued.*)

| | Emitting State[a] | | | | |
| | Band A | Band B | | Band C | Average |
Assignment ($\lvert j, n_j \rangle$)		$\Delta v = 0$	$\Delta v = -2$		
$7_3 + \lvert \frac{1}{2}, 5 \rangle$	$\cdots$	$\cdots$	$\cdots$	$5016(\alpha)$	5016
$7_3 + \lvert \frac{1}{2}, 6 \rangle$	$\cdots$	$\cdots$	$\cdots$	5141	5141
$7_3 + \lvert \frac{1}{2}, 7 \rangle$	$\cdots$	$\cdots$	$\cdots$	u	$\cdots$

[a]u denotes unresolved transitions. The labels ($\alpha - \zeta$) for the emission from band A and α for the emission (from band C) of the $\tilde{A}\,^2E_3''$ electronic state refer to transitions to combinations of the $\tilde{X}\,^2E_2''$ state levels of the vibrational mode ω_7 and the e_3' Jahn-Teller active levels. The labels ($\eta - \kappa$) for the emission from band A and ($\beta - \zeta$) for the emission from band C of the $\tilde{A}\,^2E_3''$ electronic state refer to transitions to combinations of the $\tilde{X}\,^2E_2''$ state levels of the vibrational modes ω_7 and ω_2. The estimated experimental error is ≈ 10 cm^{-1}.

[b]Since $\Delta\omega = 0$, the transition originates in level 14^2 of the $\tilde{A}$ electronic state.

[c]Possible shoulder.

[d]The transitions to the combinations between the ω_7 energy levels and the $\lvert \frac{1}{2}, n_j \rangle$ Jahn-Teller levels with $n_j = 2-4$ and $8-11$ of the $\tilde{X}$ electronic state are observed either resolved and at an expected frequency or are unresolved.

[e]The transition to its first overtone is expected in a congested energy region and is unresolved. The transitions to the combinations between its fundamental and the Jahn-Teller levels of the $\tilde{X}$ electronic state are observed either resolved and at an expected frequency or are unresolved.

[f]Dual assignment, 11_2.

[g]Tentative assignment.

[h]Dual assignment, $2_1 + \lvert \frac{1}{2}, 5 \rangle$.

modes in the $\tilde{A}\,^2E_3''$ state and including only the modes ω_{16}, ω_{17}, and ω_{18} since the Jahn-Teller effect in ω_{15} is negligible.

The assignment of the transitions to the e_3' Jahn-Teller vibronic energy levels started with a simulation [Fig. 7(B)] of the spectrum using the *ab initio* calculated parameters of the $\tilde{X}\,^2E_2''$ electronic state of C_7H_7, listed in the second and third columns of Table I. The most intense feature to the red of the origin of the simulation in Fig. 7(B) must reasonably correlate with the third most intense feature of the experimental spectrum at 1893 cm^{-1}. The only other possible candidates for assignment are the transitions to the overtone levels 2_2 and 8_2 of the $\tilde{X}$ electronic state, which we do not favor as their theoretically predicted frequencies are relatively poor matches with the experiment. The assignment is also consistent with the experimental observation in the emission from band C of the $\tilde{A}$ electronic state.

The next feature to the red in the experimental trace (at 2013 cm^{-1}) should correlate with the transition to the next member of the $j = \frac{1}{2}$ Jahn-Teller progression. Such an assignment is consistent with the experimental observation in the emissions from bands B and C. The alternative assignments to overtone transitions to the levels 7_2 (theoretically predicted frequency neglecting anharmonicity at 2028 cm^{-1}) and 19_2 of the $\tilde{X}$ electronic state are not favored since alternative assignments for these transitions are more probable (see below). Hence, the feature at 2013 cm^{-1} is assigned as a transition to the e_3' Jahn-Teller vibronic levels of the $\tilde{X}$ electronic state.

The predicted small intensity of the next Jahn-Teller feature of the simulation makes it impossible for assignment to the intense experimental feature centered at 2100 cm^{-1}. The alternative assignment to the weak band at 2180 cm^{-1} is re-

jected as there is a stronger candidate for it which also explains why it is observed in the emission from bands A and B and not in the emission from band C (*vide infra*). We conclude that this feature is experimentally unresolved due to the band peaking at 2100 cm^{-1}.

Based on the above assignments to the e_3' Jahn-Teller vibronic energy levels and a number of others (described below and in the third column of Table VI), the Jahn-Teller parameters were adjusted accordingly [see Fig. 7(C)]. We iteratively refined the theoretically calculated Jahn-Teller coupling parameters of the $\tilde{X}$ electronic state. The fifth and sixth columns of Table I summarize the experimental Jahn-Teller parameters of the $\tilde{X}\,^2E_2''$ electronic state, while the second column of Table VI lists the calculated energies of the e_3' Jahn-Teller levels based on the best-fit Jahn-Teller parameters of the $\tilde{X}\,^2E_2''$ electronic state.

With the "experimental" Jahn-Teller parameters we can actually identify a total of ten transitions (including 0_0^0) which we ascribe to the e_3' $\lvert \frac{1}{2}, n \rangle$ series. The features at 927, 1374, 1617, 1893, and 2013 cm^{-1} may be attributed to transitions to $\lvert \frac{1}{2}, n_j \rangle$ levels of the $\tilde{X}\,^2E_2''$ electronic state with $n_j = 2-6$, respectively. The transition to level $\lvert \frac{1}{2}, 7 \rangle$ is experimentally unresolved in the emission from bands A and C, but resolved in the emission from band B at 2146 cm^{-1}. The experimental features at 2340 and 2787 cm^{-1} may be attributed to transitions to levels $\lvert \frac{1}{2}, 8 \rangle$ and $\lvert \frac{1}{2}, 11 \rangle$ of the $\tilde{X}$ electronic state, though they are both predicted with small intensity, but no other alternative assignments could be made to explain these features. The transition to level $\lvert \frac{1}{2}, 10 \rangle$ may explain the band at 2530 cm^{-1} which, however, may also be attributed to a transition to level 11_2 of the $\tilde{X}\,^2E_2''$ electronic state. No plausible experimental assignment could be made
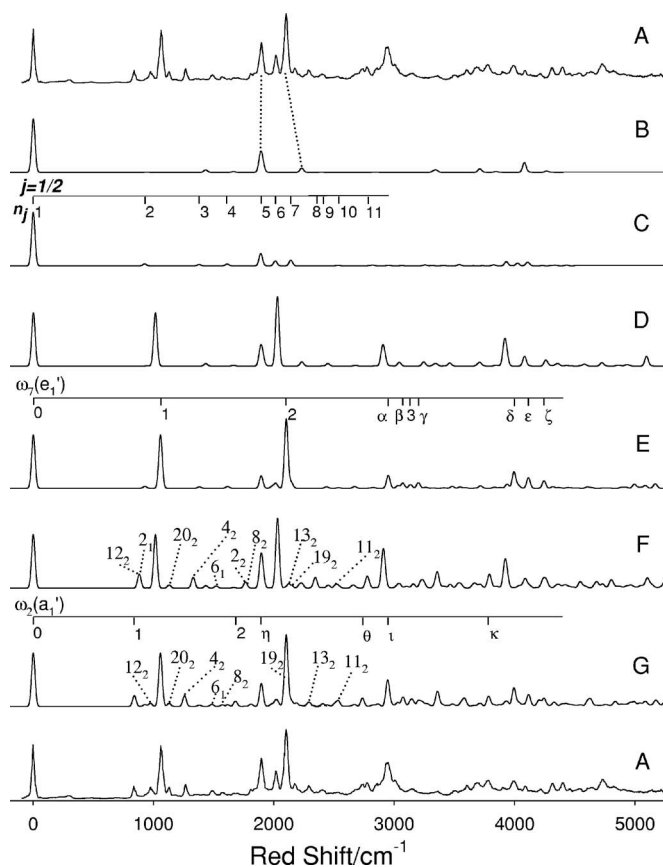
FIG. 7. LEDF spectrum of C_7H_7, excited to the vibrationless level of the $\widetilde{A}\,^2E_3''$ electronic state (band A). (A) Experimental trace (top and bottom traces). (B) Positions of the transitions to the e_3' Jahn-Teller active levels with $j=\frac{1}{2}$ symmetry, computed using the *ab initio* calculated Jahn-Teller parameters of the $\widetilde{X}\,^2E_2''$ electronic state. (C) Same as (B) but using the best-fit Jahn-Teller parameters of the $\widetilde{X}\,^2E_2''$ electronic state. (The first 11 members of the $j=\frac{1}{2}$ progression are shown.) (D) Same as (B) plus the positions of the transitions to the fundamental of e_1' of ω_7 and its first and second overtones (labeled in E as 1–3), as well as their combinations (labeled in E as $\alpha,\beta,\gamma,\delta,\varepsilon,\zeta$) with the e_3' Jahn-Teller active levels. The intensities of the transitions to the fundamental, first, and second overtones of ω_7 were adjusted to the experiment. (E) Same as (D) but using the experimentally determined parameters of the $\widetilde{X}\,^2E_2''$ electronic state. (F) Same as (D) plus the positions of the transitions to levels built on $\omega_2, \omega_4, \omega_6, \omega_8, \omega_{10}, \omega_{11}, \omega_{12}, \omega_{13}, \omega_{14}, \omega_{19}$, and ω_{20} (labeled in F and G, frequencies obtained from the *ab initio* computations of Ref. 10), their combinations with the Jahn-Teller active levels, as well as their combinations among themselves and with the ω_7 energy levels. (The combinations built on ω_7 and ω_2 are labeled in G as $\eta, \theta, \iota, \kappa$.) The intensities of the transitions to the fundamental and first overtones of ω_2, the fundamental of ω_6 and ω_{13}, as well as the first overtones of $\omega_4, \omega_8, \omega_{10}, \omega_{11}, \omega_{12}, \omega_{13}, \omega_{14}, \omega_{19}$, and ω_{20} were adjusted to the experimental observation. (G) Simulated emission spectrum obtained by using the experimentally determined parameters of the $\widetilde{X}\,^2E_2''$ electronic state. To obtain G, the calculated frequencies of F were replaced by ones that best simulated the spectrum.

TABLE VI. Calculated and experimentally observed Jahn-Teller transitions to the $|\frac{1}{2},n_j\rangle$ levels of the $\widetilde{X}\,^2E_2''$ electronic state of C_7H_7. [The calculated emission frequencies are based on the best-fit Jahn-Teller parameters of the $\widetilde{X}\,^2E_2''$ electronic state. All levels with $n_j \lesssim 11$ except the one with $n_j=9$ were used in the fit which included the six parameters $D_{16}, \omega_{16}, D_{17}, \omega_{17}, D_{18}$, and ω_{18}. The fit had a root-mean-square (rms) error of ≈ 4 cm^{-1}].

n_j	Calc.	Expt.
1	0	0
2	926	926
3	1379	1376
4	1612	1617
5	1892	1894
6	2013	2013
7	2142	2146
8	2340	2340
9	2425	⋯
10	2534	2530
11	2790	2786

assignment to a transition to the fundamental of $\omega_7(e_1')$ (theoretically predicted harmonic frequency at 1014 cm^{-1}) is the first most intense feature, 1059 cm^{-1} to the red of the origin. An alternative assignment to transitions to the $\widetilde{X}$-state level 20_2 overtone is possible but less likely due to the intensity of the band. By making this assignment, further adjustment of its position to the experiment, and assuming for ω_7 an anharmonicity constant of 6 cm^{-1}, a good match in position is achieved between the predicted transitions for the next three members of the progression and the experimentally observed features, including the ones at 2100 cm^{-1} (assigned to 7_2^0 and observed in the emission from bands A to C), at 3122 cm^{-1} (7_3^0, observed in the emission from bands A to C, resolved in the emission from bands B and C), and at 4125 cm^{-1} (7_4^0, observed in the emission from band C). The intensities of these bands are adjusted to the experiment in Fig. 7(D). Note their intensity variations across the emission spectra from bands A to C in Figs. 7 and 8. Our simulations reproduce these variations in intensity.

We first assigned features in emission from the A and C levels of the $\widetilde{A}\,^2E_3''$ electronic state; we then used the best-fit parameters of the $\widetilde{A}$ state, and in the $\widetilde{X}$-state simulation of their emissions, we found the following. The transition to the first member of the ω_7 vibrational progression of the $\widetilde{X}\,^2E_2''$ electronic state was predicted, in the emission from band A, with a strong relative intensity, while in the emission from band C with depleted intensity. The exact opposite was observed for the transition to the third member of the ω_7 progression in the simulations of the emission spectra from bands A and C. While the average of the calculated intensities of the transition to the second member of the progression in the emissions from A and C approximates the corresponding experimental one, the relative intensity is predicted opposite to the experiment (likely due to the neglect of the off-diagonal Franck-Condon factors in the theoretical model). The transition to the fourth member of the ω_7 vibronic progression is predicted with depleted relative intensity in the simulation of the emission from band A, while the

to the transition to level $|\frac{1}{2},9\rangle$ of the $\widetilde{X}$ electronic state, which was also predicted to have very weak intensity.

As indicated above, transitions may also be expected to modes $(\omega_5,\omega_6,\omega_7)$ which are linearly Jahn-Teller active in the $\widetilde{A}$ state. Figure 7(D) combines the previously discussed transitions to the $j=\frac{1}{2}$ levels plus those terminating in the $\omega_7(e_1')$ levels and their combinations with the e_3' Jahn-Teller levels, as predicted by the *ab initio* calculation of the $\widetilde{X}\,^2E_2''$ electronic state. The only logical experimental candidate for
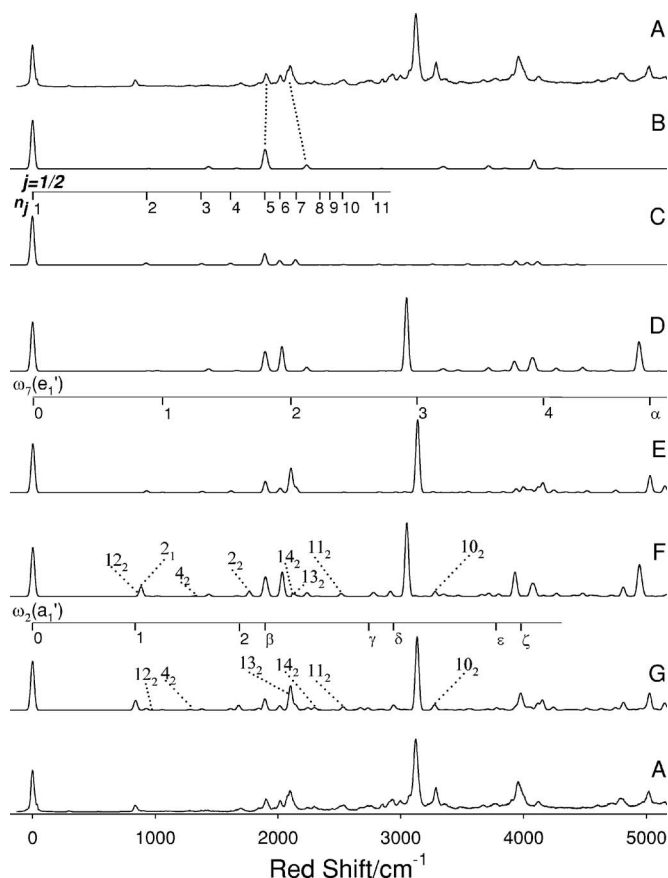
FIG. 8. LEDF spectrum of C_7H_7, excited to the $|\frac{1}{2},2\rangle$ Jahn-Teller level of the $\tilde{A}\,^2E_3''$ electronic state (band C). (A) Experimental trace (top and bottom traces). (B) Positions of the transitions to the e_3' Jahn-Teller active levels with $j=\frac{1}{2}$ symmetry, computed using the *ab initio* calculated Jahn-Teller parameters of the $\tilde{X}\,^2E_2''$ electronic state. (C) Same as (B) but using the best-fit Jahn-Teller parameters of the $\tilde{X}\,^2E_2''$ electronic state. (The first 11 members of the $j=\frac{1}{2}$ progression are shown.) (D) Same as (B) plus the positions of the transitions to the fundamental of ω_7 and its first, second, and third overtones (labeled in E as 1–4), as well as their combinations (labeled in E as α) with the Jahn-Teller active levels. The intensities of the transitions to the fundamental, first, second, and third overtones of ω_7 were adjusted to experiment. (E) Same as (D) but using the experimentally determined parameters of the $\tilde{X}\,^2E_2''$ electronic state. (F) Same as (D) plus the positions of the transitions to levels built on ω_2, ω_4, ω_{10}, ω_{11}, ω_{12}, ω_{13}, and ω_{14} (labeled in F and G, frequencies obtained from the *ab initio* computations of Ref. 10), their combinations with the Jahn-Teller active levels, as well as their combinations among themselves and with the ω_7 energy levels. (The combinations built on ω_7 and ω_2 are labeled in G as $\beta, \gamma, \delta, \varepsilon, \zeta$.) The intensities of the transitions to the fundamental and first overtone of ω_2 as well as the first overtones of ω_4, ω_{10}, ω_{11}, ω_{12}, ω_{13}, and ω_{14} were adjusted to the experimental observation. (G) Simulated emission spectrum obtained by using the experimentally determined parameters of the $\tilde{X}\,^2E_2''$ electronic state in (F).

corresponding one in the emission from band C is predicted with small but not negligible intensity, in agreement with the experiment.

Figure 7(E) displays these results. It is constructed from $j=\frac{1}{2}$ levels, $\omega_7(e_1')$ levels, and their combinations with the e_3' Jahn-Teller levels and is calculated based on the experimental spectral parameters of the $\tilde{X}\,^2E_2''$ electronic state. The $\tilde{A} \rightarrow \tilde{X}$ transitions to the energy levels of the first three quanta of excitation of $\omega_7(e_1')$ are marked 1–3 in Fig. 7(E). The transitions to the combinations between the first two mem-

bers of the $\omega_7(e_1')$ progression and the Jahn-Teller $|\frac{1}{2},n_j\rangle$ levels with $n_j=5-7$ are depicted in the figure with the Greek letters $(\alpha-\zeta)$ (see also Table V).

However, the structure in Fig. 7(E) still only accounts for part of the experimental spectrum. The band at 838 cm^{-1} in the emission from band A can be assigned to the fundamental of the ring-breathing mode ω_2. This feature is observed at the average frequency of 840 cm^{-1} in the emissions from bands A to C. The $\tilde{A}$-state fundamental frequency of ω_2 has previously been determined at 858 cm^{-1}, reasonably close to the 840 cm^{-1} value. If we assume that the potential of the vibrational mode ω_2 is harmonic in the $\tilde{X}$ state, its first overtone would be placed at 1680 cm^{-1}. Indeed, we observe a transition at this frequency in the emissions from bands A to C. As a final piece of evidence, we observe the transitions to the combinations between the ω_2 vibrational levels and the ω_7 vibrational levels of the $\tilde{X}$ electronic state in the emission from bands A to C. As there is a progression in the ring-breathing mode in the $\tilde{X}\,^2E_2''$ electronic state, then the D_{7h} ring must have a different size between the $\tilde{A}\,^2E_3''$ and $\tilde{X}\,^2E_2''$ states of C_7H_7. Indeed, the theoretical calculations of Part I have predicted a difference of 0.026 Å in the C–C bond lengths between the $\tilde{X}\,^2E_2''$ and $\tilde{A}\,^2E_3''$ state D_{7h} geometries of C_7H_7.

The weak feature at 974 cm^{-1} observed in the emission trace from band A (also observed in the emission from band B) is tentatively assigned as a transition to level 12_2 of the $\tilde{X}\,^2E_2''$ electronic state. This transition is about the only candidate for assignment and its small intensity reflects the small quadratic Jahn-Teller activity of $\omega_{12}(e_2')$ in the $\tilde{X}\,^2E_2''$ electronic state. Assignment to this feature produces an experimental frequency for the $\tilde{X}$-state fundamental of ω_{12} of 487 cm^{-1}, assuming a harmonic potential. Note that the transition to the combination between its first overtone with the fundamental of ω_2 is also observed in the emission spectra from bands A to C at 1806 cm^{-1}.

The weak feature at 1128 cm^{-1} is observed only in the emission from band A. It is assigned to a transition to level 20_2 based on the good agreement with the theoretically predicted frequency of (564×2) cm^{-1}. The transition to the combination between its first overtone and the fundamental of ω_7 is also observed in the emission spectra from bands A and B at the average frequency of 2184 cm^{-1}.

The feature at 1261 cm^{-1} in the emission from band A is attributed to the transition 4_2^0 (theoretical frequency at 1328 cm^{-1}). The vibrational frequency analysis of Part I has predicted that non-negligible off-diagonal Franck-Condon factors are to be expected for ω_4. The average experimental frequency of its fundamental in the $\tilde{X}\,^2E_2''$ state, neglecting anharmonicity, is 632 cm^{-1}, while the corresponding one in the $\tilde{A}\,^2E_3''$ state is 677 cm^{-1}. The $\tilde{A}\rightarrow\tilde{X}$ transition to the combination level 4_2+12_2, in the emission spectra from bands A to C, is observed at 2242 cm^{-1} and the one to 4_2+7_1, in the emission spectra from bands A and B, is unresolved.

The band at 1482 cm^{-1} in the emission from band A is assigned as a transition to the fundamental of $\omega_6(e_1')$ in the $\tilde{X}\,^2E_2''$ state (theoretically predicted harmonic frequency at

TABLE VII. Experimentally determined vibrational frequencies for $\widetilde{X}$ and $\widetilde{A}$ states of C_7H_7 using D_{7h} notation and the corresponding calculated frequencies (see Part I for details) for $C_7H_7^+$ at D_{7h} symmetry. (The harmonic vibrational frequencies are not scaled. The symmetry of the vibrational modes in the second column is given in the D_{7h} group. The Herzberg numbering scheme is used to label the vibrations.)

| Mode | Symmetry | $C_7H_7^+$ $\widetilde{X}\,^1A_1'$ Calc. | | | C_7H_7 | |
		RHF	MP2	(B3LYP)[a]	$\widetilde{X}\,^2E_2''$ Expt.[b]	$\widetilde{A}\,^2E_3''$ Expt.[b]
1	a_1'	3383	3254	3210	⋯	⋯
2	a_1'	937	874	881	840	858[c]
3	a_2'	1559	1417	1441	⋯	⋯
4	a_2''	730	651	664	632[d]	677[c]
5	e_1'	3378	3250	3205	⋯	⋯
6	e_1'	1641	1495	1519	1482	⋯
7	e_1'	1082	1009	1014	1060	⋯
8	e_1''	978	866	891	788[d]	849[d]
9	e_2'	3366	3240	3196	⋯	⋯
10	e_2'	1777	1624	1637	1643	1699[d]
11	e_2'	1339	1247	1255	1265[d]	1191[d]
12	e_2'	469	428	438	487[d]	⋯
13	e_2''	1171	988	1061	1144[d–f]	1032[d,e]
14	e_2''	247	212	224	208[d]	294[d]
15	e_3'	3356	3229	3187	⋯	⋯
16	e_3'	1611	1721	1568	⋯	1545[c]
17	e_3'	1377	1302	1313	⋯	1253[c]
18	e_3'	941	895	898	⋯	857[c]
19	e_3''	1193	992	1079	1040[d,e]	1104[d–f]
20	e_3''	606	537	564	564[d]	⋯

[a]Pino *et al.* (Ref. 2) determined the harmonic vibrational frequencies of $C_7H_7^+$ in its $\widetilde{X}\,^1A_1'$ electronic state at the B3LYP/6-31G** level of theory and produced results consistent with this work.
[b]Determined from the LIF and LEDF spectra.
[c]Experimental frequency of a fundamental level which is part of a combination band.
[d]Experimental frequency determined by taking one-half of the frequency of the overtone.
[e]Tentative assignment.
[f]This vibrational mode may likely have large contributions from anharmonicity terms.

1519 cm^{-1}) and allowed by Jahn-Teller activity in the $\widetilde{A}\,^2E_3''$ state. This feature is also observed in the emission from band B. No other candidate for assignment is likely based on the theoretical prediction. The transition to its first overtone is expected at 2964 cm^{-1}, neglecting anharmonicity, but is located in a congested energy region and is unresolved. A transition assignable to $6_1+|\frac{1}{2},2\rangle$ is observed in the emission from bands A and B at the average frequency of 2408 cm^{-1}.

The weak feature at 1577 cm^{-1} is observed in the emission from bands A and B and is attributed to the 8_2 level of the $\widetilde{X}\,^2E_2''$ state. Non-negligible off-diagonal Franck-Condon factors are expected for $\omega_8(e_1'')$ based on the vibrational frequency analysis of Part I.

The peak at the average frequency of 2081 cm^{-1} (resolved in the emissions from bands B and C) is assigned to transition 19_2^0. The only other alternative assignment is 13_2^0 which is less favored due to a poorer frequency match to the calculated frequency neglecting anharmonicity of 1040 cm^{-1} which further indicates small but non-negligible off-diagonal Franck-Condon factors. Assuming the correctness of this assignment, we conclude that the potential of $\omega_{13}(e_2'')$ must be anharmonic in the $\widetilde{A}$ state as this vibrational mode is subject only to small quadratic Jahn-Teller interactions in the $\widetilde{X}\,^2E_2''$ state.

The band at 2288 cm^{-1} (observed in the emission from bands A to C) is attributed to transition 13_2^0. The experimental frequency for the fundamental level of $\omega_{13}(e_2'')$ in the $\widetilde{X}\,^2E_2''$ electronic state is 1144 cm^{-1}. Finally, the feature at 2530 cm^{-1} (observed in the emission from bands A to C) is therefore attributable to the transition to level 11_2 of the $\widetilde{X}\,^2E_2''$ state. Its experimental fundamental frequency in the $\widetilde{X}$ state, assuming no anharmonicity, is 1265 cm^{-1}, while the corresponding one in the $\widetilde{A}$ state is 1191 cm^{-1}. As the vibrational mode $\omega_{11}(e_2')$ exhibits small quadratic Jahn-Teller activity in the $\widetilde{X}\,^2E_2''$ state, the observed small line intensity in the ground state (and/or excited state) vibronic spectrum of C_7H_7 may be due to anharmonicity effects.

The information contained in Fig. 7(D) plus the positions of the above discussed transitions to the levels built on ω_2, ω_4, ω_6, ω_8, ω_{10}, ω_{11}, ω_{12}, ω_{13}, and ω_{20} (labeled in F and G), their combinations with the Jahn-Teller active levels, as well as their combinations among themselves and with the ω_7 energy levels are included in Fig. 7(F). This simulation is calculated based on the theoretical spectral parameters of the $\widetilde{X}\,^2E_2''$ state. The intensities of the transitions were adjusted to the experiment.

Our final simulated emission spectrum [Fig. 7(G)] con-

TABLE VIII. Calculated and experimentally determined linear Jahn-Teller coupling constants for the $\tilde{X}\,^2E_1''$ electronic state of C_5H_5, $\tilde{X}\,^2E_{1g}$ electronic state of $C_6H_6^+$, and $\tilde{X}\,^2E_2''$ and $\tilde{A}\,^2E_3''$ electronic states of C_7H_7. (All constants have units of cm^{-1} except D_i's which are unitless. The latter parameters were theoretically computed using method II of Ref. 17.)

Symmetry coordinate		$C_5H_5\ \tilde{X}\,^2E_1''$ Theory[a]	Expt.[a]		$C_6H_6^+\ \tilde{X}\,^2E_{1g}$ Theory[b]	Expt.[b]		$C_7H_7\ \tilde{X}\,^2E_2''$ Theory[c]	Expt.[d]		$C_7H_7\ \tilde{A}\,^2E_3''$ Theory[c]	Expt.[d]
C–C–C bend	D_{12}	0.22	0.19	D_{18}	0.42	0.51	D_{18}	0.013	0.09			
	$\omega_{e,12}$	817	872	$\omega_{e,18}$	573	584	$\omega_{e,18}$	941	900			
	ε_{12}	176	166	ε_{18}^0	246	306	ε_{18}	12	81			
C–C–H bend	D_{11}	0.34	0.57	D_{17}	0.12	0.12	D_{17}	0.295	0.12	D_7	1.098	0.70
	$\omega_{e,11}$	1061	1041	$\omega_{e,17}$	1152	1161	$\omega_{e,17}$	1377	1350	$\omega_{e,7}$	1082	950
	ε_{11}	361	594	ε_{17}^0	138	136	ε_{17}	406	162	ε_7	1188	665
C–C stretch	D_{10}	0.68	0.36	D_{16}	0.23	0.18	D_{16}	0.589	0.50	D_6	0.102	0.10
	$\omega_{e,10}$	1415	1320	$\omega_{e,16}$	1571	1543	$\omega_{e,16}$	1611	1600	$\omega_{e,6}$	1641	1519
	ε_{10}	934	477	ε_{16}^0	364	265	ε_{16}	949	800	ε_6	167	152
C–H stretch	D_9	<0.01	⋯	D_{15}	<0.01	⋯	D_{15}	0.002	⋯	D_5	0.004	⋯
	$\omega_{e,9}$	3040	⋯	$\omega_{e,15}$	3017	⋯	$\omega_{e,15}$	3356	⋯	$\omega_{e,5}$	3378	⋯
	ε_9	<1	⋯	ε_{15}^0	<1	⋯	ε_{15}	7	⋯	ε_5	13	⋯
ε_T[e]		1497[f]	1237		757[g]	707		1374	1043		1368	817

[a]See Refs. 17 and 24. The components of the distortion vector were calculated at the CASSCF/6-31G* level of theory, while the harmonic vibrational frequencies and the vectors pointing along the normal coordinates of the linear Jahn-Teller active vibrations at X_0 were calculated at the GRHF/6-31G* level of theory.

[b]See Ref. 14. The distortion-vector components as well as the harmonic vibrational frequencies and the vectors along the normal coordinates of the linear Jahn-Teller active vibrational modes at X_0 were determined at the CASSCF/6-31G* level of theory.

[c]Present work. For the C_7H_7 $\tilde{X}\,^2E_2''$ and $\tilde{A}\,^2E_3''$ electronic states, the distortion-vector components were computed at the EOMEA-CCSD/TZ2P level of theory, while the harmonic vibrational frequencies as well as the vectors pointing along the normal coordinates of the linear Jahn-Teller active vibrational modes at X_0 were computed at the RHF/6-31G** level of theory.

[d]Experimental linear Jahn-Teller coupling constants taken from Part II.

[e]The total Jahn-Teller energy stabilizations were determined using method II of Ref. 17.

[f]The differences in ε_T and the sum of ε_i is due to the round-off error in ε_i.

[g]The energy difference of 9 cm^{-1} between ε_T and the sum of ε_i^0 corresponds to the barrier to pseudorotation around the $\tilde{X}$-state PES moat.

tains the same information as Fig. 7(F) but is constructed based on the experimentally determined spectral parameters of the $\tilde{X}\,^2E_2''$ electronic state. There seems to be a one-to-one correspondence between the experimentally observed features and the simulated ones in Fig. 7(G). The spectroscopic labels of all of the above "assignments" are summarized in the first column of Table V.

2. Emission from band C of the Ã electronic state of C_7H_7

We briefly review the emission from band C, which corresponds from the transition to the e_1' Jahn-Teller level $|\frac{1}{2},2\rangle$ of the $\tilde{A}\,^2E_3''$ electronic state. The majority of the spectral features observed in the emission from band C are also observed in the emission through the origin of the excitation spectrum, namely, band A.

The experimental spectrum is given in Fig. 8(A). Our Jahn-Teller simulation is presented in Fig. 8(B). Jahn-Teller levels of $j=\frac{1}{2}$ symmetry are computed based on the theoretically calculated Jahn-Teller parameters of the $\tilde{X}\,^2E_2''$ electronic state (see Table I). Figure 8(C) includes the same transition as Fig. 8(B) but it is constructed using the best-fit

Jahn-Teller parameters of the $\tilde{X}\,^2E_2''$ state. The first 11 members of the $j=\frac{1}{2}$ vibronic progression are shown.

Figure 8(D) includes the same transitions as Fig. 8(B) plus the positions of the transitions to the fundamental of ω_7 and its first, second, and third overtones (labeled in E as 1–4), as well as the latter's combination (labeled in E as α) with the Jahn-Teller active level. The intensities of the transitions to the fundamental, first, second, and third overtones of ω_7 were adjusted to the experiment. Figure 8(E) contains the same transitions as Fig. 8(D) but is based on the experimentally determined parameters of the $\tilde{X}\,^2E_2''$ electronic state.

Figure 8(F) contains the same transitions as Fig. 8(D) plus the positions of the transitions to levels built on ω_2, ω_4, ω_{10}, ω_{11}, ω_{12}, ω_{13}, and ω_{19} (labeled in F and G), their combinations with the Jahn-Teller active levels, as well as their combinations among themselves and with the ω_7 energy levels. The intensities of the transitions to the fundamental and first overtone of ω_2 as well as the first overtones of ω_4, ω_{10}, ω_{11}, ω_{12}, ω_{13}, and ω_{14} were adjusted to the experiment.

Finally, Fig. 8(G) shows the corresponding spectrum obtained by using the experimentally determined parameters of the $\tilde{X}\,^2E_2''$ electronic state. These are experimentally deter-
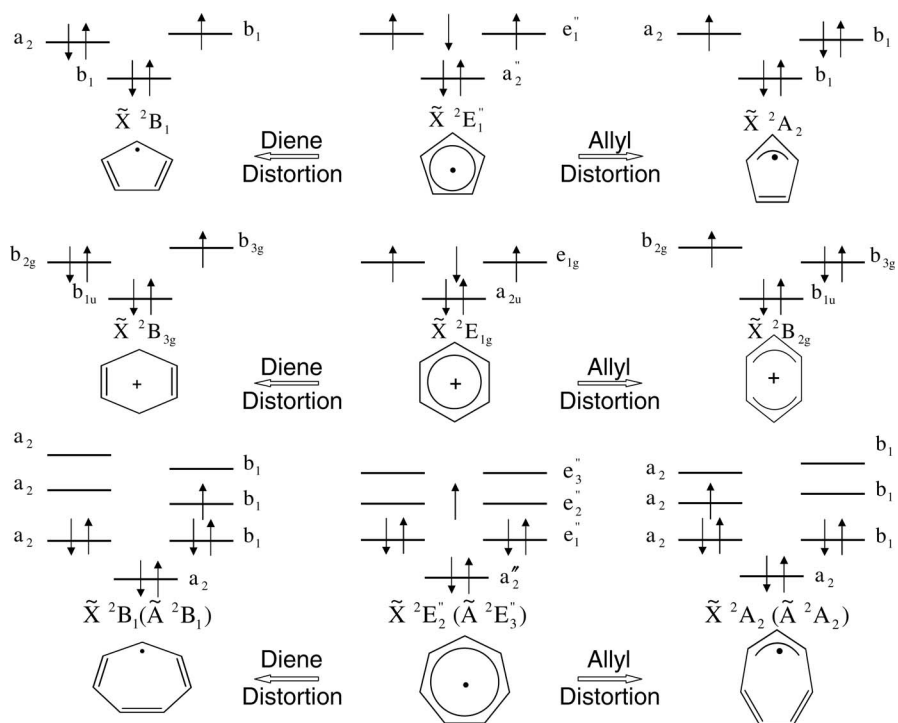
FIG. 9. Schematic diagram showing dominant electronic configurations for the $\widetilde{X}$ states of C_5H_5, $C_6H_6^+$, and C_7H_7. The effects of Jahn-Teller distortion of the orbitals and the geometry of tropyl are indicated. For the $\widetilde{A}$ state of C_7H_7, the "unpaired" electron is promoted to the e_3'' orbital which again decomposes into A_2 and B_1 states upon distortion.

mined from the totality of data from the LEDF spectra from bands A, B, and C and are summarized in Tables VII and VIII.

V. DISCUSSION

One of the major motivations for the present work was to extend our previous work on the C_nH_n family of Jahn-Teller active, quasi-aromatic hydrocarbon rings from $n=5$ and 6 to include 7. We additionally wanted to examine the capability of modern *ab initio* calculations to predict PESs that were compatible with the ones obtained from the spectral analysis. Furthermore, we wanted to observe whether there were systematic effects in PESs as the rings grow larger. To facilitate these comparisons, Fig. 9 schematically represents the radicals at the high symmetry (D_{7h}) conical intersection and at their distorted minima (C_{2v}). In addition, the dominant electronic configuration is presented for each of the molecular structures.

In Table VII, we compare the calculated frequencies (at D_{7h} symmetry) with the experimentally determined ones for both Jahn-Teller active and non-Jahn-Teller active modes. As can be seen from Table VII, there is generally good agreement between the experimental and calculated frequencies, particularly the B3LYP ones, for both the $\widetilde{X}$ and $\widetilde{A}$ states.

Table VIII compiles the theoretically calculated (using method II of Ref. 17) and experimentally determined linear Jahn-Teller coupling constants for the $\widetilde{X}\,^2E_1''$ (D_{5h}) electronic state of C_5H_5, $\widetilde{X}\,^2E_{1g}$ (D_{6h}) electronic state of $C_6H_6^+$, and $\widetilde{X}\,^2E_2''$ and $\widetilde{A}\,^2E_3''$ (D_{7h}) electronic states of C_7H_7. The linear Jahn-Teller active vibrational modes for each molecular species are labeled according to their most important symmetry coordinate, which is given in the first column. The third column lists the theoretically computed C_5H_5 harmonic vibrational frequencies of the four e_2' linearly Jahn-Teller active

vibrations ($\omega_9 - \omega_{12}$), as well as their corresponding linear Jahn-Teller coupling constants and Jahn-Teller stabilization energies ε_i. The fourth column presents the corresponding experimental molecular parameters. A similar pattern of presentation is followed for $C_6H_6^+$ and C_7H_7. The last row of Table VIII gives the total Jahn-Teller energy stabilizations ε_T that were theoretically computed and experimentally determined for the C_nH_n PESs.

The easiest thing to compare is the total Jahn-Teller stabilization energy ε_T which is plotted in Fig. 10 as a function of n. It is clear that the calculations modestly overestimate the stabilization for all n; however, the difference with experiment is clearly smallest for the even carbon atom radical cation. This systematic overestimation of the empirical stabilization by the calculations has previously[18–20] been noted for C_5H_5 and $C_6H_6^+$ as well as for the related species[21] $C_6F_6^+$. However, from Fig. 10, it is clear that the calculations rather faithfully track the empirical variation of ε_T as a function of n, including the significant dip for the cation.

It is also interesting to note the variation in ε_T as n increases. It can be argued that as the number of carbon atoms increases to infinity, one reaches the limit of cylindrical symmetry for which the linear Jahn-Teller effect vanishes for any E_m electronic state with $m>1$. Although the dip for the cation complicates matters, the data in Table VIII support the idea that ε_T decreases as n and m move toward that limit.

The excited $\widetilde{A}$ state of C_7H_7 offers further insight into the qualitative behavior of the Jahn-Teller effect. One notes from Table VIII that experimentally there is a clear decrease in ε_T as one goes from the $\widetilde{X}$ to the $\widetilde{A}$ state. The calculations also indicate a decrease but it is so small that it is not numerically significant. From Fig. 9, the "unpaired" electron is predominately in an e_2'' orbital in the $\widetilde{X}$ state, while it is in an e_3'' orbital in the $\widetilde{A}$ state. It has been suggested that states, E_i,
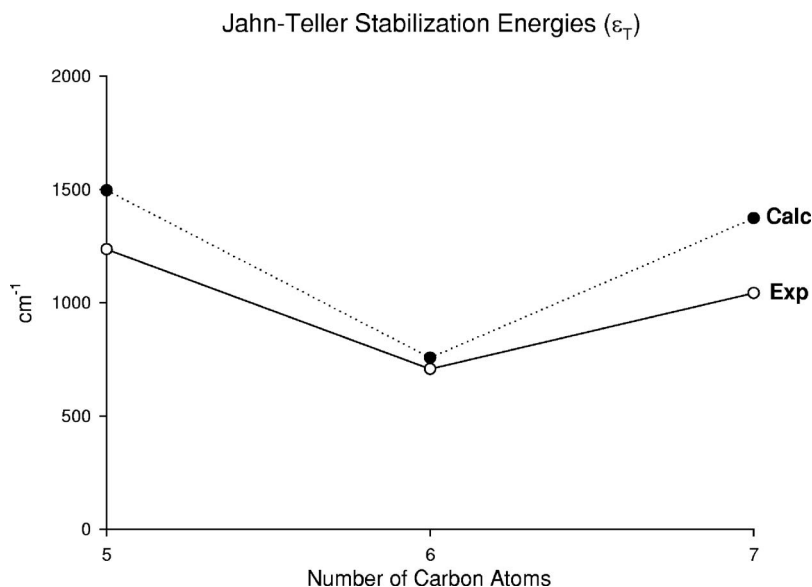
FIG. 10. Plot of the $\tilde{X}$-state total Jahn-Teller stabilization energies ε_T (experimental and theoretical) of the C_nH_n Jahn-Teller active molecules vs the number of carbon atoms.

with larger values of i should show smaller linear Jahn-Teller effects.[22,23] The experimental results appear to be consistent with this argument, although previous work[23] on the $\tilde{B}\,^2E_{2g}$ state of $C_6H_6^+$ has not confirmed it. However, a somewhat simpler physical argument may explain the observations as well. As the unpaired electron is promoted to a higher energy orbital, the state becomes more Rydberg-like, with the limit being the closed shell ion with vanishing Jahn-Teller effect.

The other area of insight offered by the present data is the nature of the geometric distortions that are responsible for the energy stabilization. The *ab initio* calculations and the experimental results are consistent with a picture of significant Jahn-Teller distortion of the C_nH_n $\tilde{X}$-state PESs along three internal coordinates: C–C–C and C–C–H bend and C–C stretch, with the C–H stretch having negligible importance. A graphical representation shown in Fig. 11 of the experimental and theoretical ε_T's gives the percentage contribution of the $\tilde{X}$-state linear Jahn-Teller active vibrational modes in the experimental and theoretical ε_T's for the C_nH_n molecules with $n=5-7$ versus the number of carbon atoms. The contribution to the experimental ε_T from the C–C stretch

vibrational mode is dominant for all the molecules and increases in going from C_5H_5 to C_7H_7, while that from the C–C–H bend vibrational mode decreases. The contribution in the experimental ε_T from the C–C–C bend vibrational mode appears to be most significant for $C_6H_6^+$, while it becomes significantly less important for the neutral radicals and nearly negligible for C_7H_7. Overall, there seems a tendency to localize the distortion in the C–C stretch as the molecule becomes larger. However, these observations must be taken in a qualitative sense since in no case does the normal mode correspond precisely to the internal coordinate. It is also interesting to note from Fig. 11 that the calculated contributions to ε_T generally track reasonably well the experimental results. This is particularly pleasing since the determination of the orientation of the normal modes is likely one of the weaker points of the calculations.

The partitioning of the ϵ_T to different distortions appears more difficult to understand when the $\tilde{A}$ state is considered. First, it should be noted that now there are only three modes that are possibly Jahn-Teller active, and from Table VIII we see that again the C–H stretch is a negligible contributor.
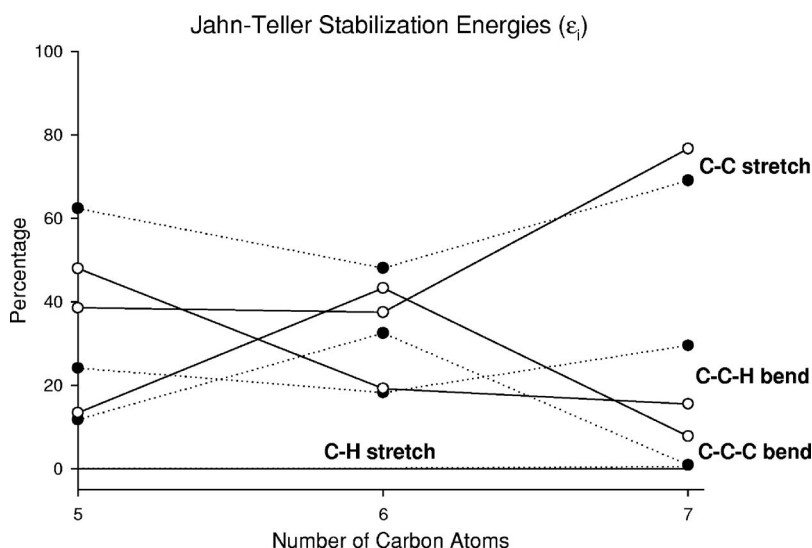

FIG. 11. Plot of the percentage contribution of the individual $\tilde{X}$-state linear Jahn-Teller active vibrational modes of the C_nH_n Jahn-Teller active molecules to the experimental (depicted by solid lines) and calculated (dotted lines) total Jahn-Teller stabilization energies ε_T vs the number of carbon atoms.

From the calculation, mode 7 is a mixture of C–C–C bend and C–C stretch, while ω_6 is a picture of C–C–C bend + C–C–H bend. Experimentally and computationally, about 80% of the ε_T comes from ω_7 which contains the C–C stretch, which is generally consistent with the observations on the ground state molecules.

VI. CONCLUSIONS

The jet-cooled, laser-excited, dispersed fluorescence emission spectra and the laser-induced fluorescence excitation spectrum of the tropyl radical have been successfully analyzed utilizing *ab initio* molecular parameters as a starting point. There is an overall good agreement between the experimental and theoretical Jahn-Teller parameters for the $\tilde{A}\ ^2E_3''$ and $\tilde{X}\ ^2E_2''$ states. The vibronic structures of the $\tilde{A}\ ^2E_3''$ and $\tilde{X}\ ^2E_2''$ electronic states reveal the Jahn-Teller distortion of their PESs. The contribution from the e_3' vibrational modes is important in the excitation spectrum and that from the e_1' vibrational modes (particularly the one that is the most Jahn-Teller active in the $\tilde{A}$ state) in the emission spectra. General trends for the Jahn-Teller parameters as a function of n are revealed for the C_nH_n molecules.

ACKNOWLEDGMENTS

[1] R. G. Satink, G. Meijer, and G. von Helden, J. Am. Chem. Soc. **125**, 15714 (2003), and references therein.

[2] T. Pino, F. Güthe, H. Ding, and J. P. Maier, J. Phys. Chem. A **106**, 10022 (2002), and references therein.

[3] E. P. F. Lee and T. G. Wright, J. Phys. Chem. A **102**, 4007 (1998), and references therein.

[4] R. D. Johnson, J. Chem. Phys. **95**, 7108 (1991), and references therein.

[5] S. K. Shin, Chem. Phys. Lett. **280**, 260 (1997).

[6] B. J. Smith and N. E. Hall, Chem. Phys. Lett. **279**, 165 (1997).

[7] H. J. Silverstone, D. E. Wood, and H. M. McConnell, J. Chem. Phys. **41**, 2311 (1964).

[8] R. F. Gunion, W. Karney, P. G. Wenthold, W. T. Borden, and W. C. Lineberger, J. Am. Chem. Soc. **118**, 5074 (1996).

[9] B. A. Thrush and J. J. Zwolenik, Faraday Discuss. Chem. Soc. **35**, 196 (1963).

[10] V. L. Stakhursky, I. Sioutis, G. Tarczay, and T. A. Miller, J. Chem. Phys. **128**, 084310 (2008).

[11] T. A. Barckholtz and T. A. Miller, Int. Rev. Phys. Chem. **17**, 435 (1998).

[12] V. L. Stakhursky, V. A. Lozovsky, C. B. Moore, and T. A. Miller, 60th International Symposium on Molecular Spectroscopy, The Ohio State University, Columbus OH, 2005 (unpublished).

[13] J. P. Maier (private communication).

[14] B. E. Applegate and T. A. Miller, J. Chem. Phys. **117**, 10654 (2002), and references therein.

[15] W. G. Fateley, B. Curnette, and E. R. Lippincott, J. Chem. Phys. **26**, 1471 (1957).

[16] F. Güthe, H. Ding, T. Pino, and J. P. Maier, Chem. Phys. **269**, 347 (2001).

[17] B. E. Applegate, T. A. Miller, and T. A. Barckholtz, J. Chem. Phys. **114**, 4855 (2001), and references therein.

[18] B. E. Applegate, T. A. Miller, and T. A. Barckholtz, J. Chem. Phys. **114**, 4855 (2001).

[19] B. E. Applegate, A. J. Bezant, and T. A. Miller, J. Chem. Phys. **114**, 4869 (2001).

[20] B. E. Applegate and T. A. Miller, J. Chem. Phys. **117**, 10654 (2002).

[21] K. Raghavachari, R. C. Haddon, T. A. Miller, and V. E. Bondybey, J. Chem. Phys. **79**, 1387 (1983).

[22] J. G. Goode, J. D. Hofstein, and P. M. Johnson, J. Chem. Phys. **107**, 1703 (1997).

[23] P. M. Johnson, J. Chem. Phys. **117**, 10001 (2002).

[24] B. E. Applegate, A. J. Bezant, and T. A. Miller, J. Chem. Phys. **114**, 4869 (2001).